TECHNISCHE UNIVERSITÄT WIEN
Vienna University of Technology

LUDWIG BOLTZMANN INSTITUTE
Traumatology
The Research Center in Cooperation with AUVA

DIPLOMARBEIT

Assessment of Peripheral Nerve Regeneration Across a 7mm gap in the Delayed Rat Median Nerve Model: A Comparative Study of Autologous Nerve Graft, Muscle Filled-in Vein Conduit, and Extracellular Vesicle-Based Therapies

Performed at the

Ludwig Boltzmann Institute for Traumatology, the Research Center in Cooperation with AUVA

and the

Institute of Chemical, Environmental and Bioscience Engineering at the Technical University of Vienna

Under the supervision of

Mag. Dr. David Hercher

a.o.Univ.Prof. Dipl.-Ing. Dr. techn. Heinz Redl

By

Maria Danen, BSc

Mat.Nr.: 12326223

Affidavit

I declare in lieu of oath, that I wrote this thesis and carried out the associated research myself, using only the literature cited in this volume. If text passages from sources are used literally, they are marked as such.

I confirm that this work is original and has not been submitted for examination elsewhere, nor is it currently under consideration for a thesis elsewhere.

Place and Date	*Signature*

Acknowledgements

First and foremost, I would like to express my sincere gratitude to Dr. David Hercher for his invaluable guidance throughout my thesis. His support, patience, and willingness to answer all my questions and think with me on problems had a significant impact on my work and learning experience. I am especially grateful to Prof. Heinz Redl for connecting me with David and helping me secure this exciting thesis project at the Ludwig Boltzmann Institute for Traumatology, where I had the opportunity to work in such a dynamic and research driven environment.

I am deeply thankful to Mag. Barbara Schädl and the rest of the histology team for their extensive help with histological processing, particularly their experience and assistance with swift preparation and practical guidance in the lab. My thanks also go to Diogo Jorge Santos, whose help in setting up the preprocessing pipeline greatly improved the quality of the segmentation results.

I would also like to acknowledge the in-vivo team who introduced me to additional in-vivo projects. Observing these was both educational and inspiring, offering me a broader perspective on the field. Special thanks to Mai Quyen Nguyen for allowing me to take part in her thesis project and for her consistent, kind support throughout our collaboration.

I am grateful to the neuroregeneration team whom I worked alongside during this time, for their collaboration, open communication, and the team spirit we shared. Staying updated on each other's progress and supporting one another was a motivating aspect of this experience.

Furthermore, I extend my appreciation to the Ludwig Boltzmann Institute for Traumatology for providing the materials, infrastructure, and welcoming atmosphere that allowed me to carry out my work effectively. The positive and collaborative environment made a real difference during the course of my thesis.

Finally, I would like to thank my friends and family for their encouragement and understanding throughout this process. Their support was essential during the more challenging moments of my academic journey.

Table of Contents

English Abstract

Peripheral nerve injuries remain a major clinical challenge, often resulting in incomplete functional recovery despite surgical intervention. Reliable preclinical models are crucial for evaluating repair strategies and understanding the biological processes that play a role in nerve repair. This study investigates treatment modalities to enhance regeneration of the median nerve following segmental injury in rats, with a focus on delayed nerve repair. In this study the autologous nerve transplant (ANT) is compared to muscle filled-in vein conduit (MVCs) after an 8-week repair delay, with or without additional treatment using extracellular vesicles (EVs), either wild-type EVs or modified EVs to enhance laminin-binding functionality. A total of 48 male Lewis rats (mean weight: 484 g) were evenly distributed across six conduit type and treatment groups (MVC = 24, ANT= 24, of which: PBS= 8, modEVs= 8 and wtEVs= 8). Twelve weeks post-repair, nerve regeneration was assessed through in-vivo electrophysiological recordings and histological analyses. Compound muscle action potentials (CMAPs) were analyzed for latency, duration, amplitude, and area under the curve. The values were compared with histological data (H&E, c-Jun, GFAP, MSB, and MBP staining). A key objective of this study was to establish a standardized pipeline for quantitative histomorphometry using MBP immunostaining in combination with AxonDeepSeg, an automated segmentation tool. This platform enabled consistent quantification of axonal and myelin structures. While EV treatments did not yield statistically significant improvements, largely due to inter-animal variability, the ANT groups demonstrated superior regenerative outcomes, as evidence by higher CMAP amplitudes and larger areas under the curve compared to MVC groups. Importantly, strong linear correlations were observed between the total number of nerve fibers and CMAP amplitude (p = 0.0002) and area under the curve (p = 0.0005). Additional significant correlations were found between CMAP duration and axon diameter (p = 0.0014), myelin thickness (p = 0.0241), and g-ratio (p = 0.0011). These findings highlight the enhanced regenerative capacity of ANT over MVC in delayed repair scenarios and validate the use of MBP staining with AxonDeepSeg as a robust method for histomorphometric analysis in peripheral nerve studies.

Deutsche Kurzfassung

Periphere Nervenverletzungen stellen nach wie vor eine große klinische Herausforderung dar und führen trotz chirurgischer Eingriffe häufig zu einer unvollständigen funktionellen Wiederherstellung. Zuverlässige präklinische Modelle sind für die Bewertung von Reparaturstrategien und das Verständnis der biologischen Prozesse, die bei der Nervenreparatur eine Rolle spielen, von entscheidender Bedeutung. Diese Studie untersucht Behandlungsmethoden zur Verbesserung der Regeneration des Nervus medianus nach segmentalen Verletzungen bei Ratten, wobei der Schwerpunkt auf der verzögerten Nervenreparatur liegt. In dieser Studie wird die autologe Nerventransplantation (ANT) mit muskelfüllten Venenkonduits (MVCs) nach einer 8-wöchigen Reparaturverzögerung verglichen, mit oder ohne zusätzliche Behandlung mit extrazellulären Vesikeln (EVs), entweder Wildtyp-EVs oder modifizierten EVs zur Verbesserung der Laminin-Bindungsfunktion. Insgesamt 48 männliche Lewis-Ratten (Durchschnittsgewicht: 484 g) wurden gleichmäßig auf sechs Conduit-Typen und Behandlungsgruppen verteilt (MVC = 24, ANT = 24, davon: PBS = 8, modEVs = 8 und wtEVs = 8). Zwölf Wochen nach der Reparatur wurde die Nervenregeneration durch in-vivo-elektrophysiologische Aufzeichnungen und histologische Analysen bewertet. Die zusammengesetzten Muskelaktionspotenziale (CMAPs) wurden hinsichtlich Latenz, Dauer, Amplitude und Fläche unter der Kurve analysiert. Die Werte wurden mit histologischen Daten (H&E-, c-Jun-, GFAP-, MSB- und MBP-Färbung) verglichen. Ein wichtiges Ziel dieser Studie war es, eine standardisierte Pipeline für die quantitative Histomorphometrie unter Verwendung der MBP-Immunfärbung in Kombination mit AxonDeepSeg, einem automatisierten Segmentierungswerkzeug, zu etablieren. Diese Plattform ermöglichte eine konsistente Quantifizierung der Axon- und Myelin Strukturen. Während die EV-Behandlungen keine statistisch signifikanten Verbesserungen ergaben, was vor allem auf die Variabilität zwischen den Tieren zurückzuführen war, zeigten die ANT-Gruppen überlegene Regenerationsergebnisse, was durch höhere CMAP-Amplituden und größere Flächen unter der Kurve im Vergleich zu den MVC-Gruppen belegt wurde. Wichtig ist, dass starke lineare Korrelationen zwischen der Gesamtzahl der Nervenfasern und der CMAP-Amplitude (p = 0,0002) sowie der Fläche unter der Kurve (p = 0,0005) beobachtet wurden. Weitere signifikante Korrelationen wurden zwischen der CMAP-Dauer und dem Axondurchmesser (p = 0,0014), der Myelindicke (p = 0,0241) und dem g-Verhältnis (p = 0,0011) festgestellt. Diese Ergebnisse

unterstreichen die verbesserte Regenerationsfähigkeit von ANT gegenüber MVC bei verzögerten Reparaturprozessen und bestätigen die Verwendung der MBP-Färbung mit AxonDeepSeg als robuste Methode für die histomorphometrische Analyse in Studien zu peripheren Nerven.

List of Figures

List of Tables

List of Abbreviations

ADS ..... AxonDeepSeg
ANT ..... Autologous nerve transplant
ASC ..... Adipose-derived stem cells
BDNF ..... Brain derived neurotrophic factor
CMAP ..... Compound muscle action potential
FDA ..... Food and Drug Administration
FDS ..... Flexor digitorum superficialis
GFAP ..... Glial fibrillary acidic protein
HIER ..... Heat induced epitope retrieval
HRP ..... Horseradish peroxidase
IHC ..... Immunohistochemistry
MAG ..... Myelin-associated glycoprotein
MBP ..... Myelin basic protein
modEV ..... Modified extracellular vesicle
MSB ..... Martius Scarlet Blue
MVC ..... Muscle filled-in vein conduit
NGF ..... Nerve growth factor
P0 ..... Myelin protein zero
PMP22 ..... Peripheral myelin protein 22
PN ..... Peripheral nerve
PNI ..... Peripheral nerve injury
PNS ..... Peripheral nervous system
PVA ..... Polyvinyl alcohol
PGA ..... Polyglycolic acid
SC ..... Schwann cell
SEM ..... Scanning electron microscopy
TEM ..... Transmission electron microscopy
wtEV ..... Wildtype extracellular vesicle

1 Introduction and Motivation

1.1 Peripheral nerve injuries

Peripheral nerve injuries (PNI) are common following blunt or penetrating trauma, accounting for 3.3% of upper extremity traumatic cases, according to data from the German TraumaRegister DGU [1]. PNIs lead to loss of sensation, movement and in many cases, chronic pain [2], [3]. Patients of work-related upper extremity PNIs are to a large extent male (85%), with the majority working the wood and metal industry (21%), construction (15%), and trade industry (14%). 66% Of these PNIs were related to median nerve injury, with increasing frequency of injuries located moving more distally to the extremity [4].

The timing and success of the peripheral nerve (PN) repair process depends on the extent of the injury. Clinical grading systems are used to match microscopic changes and patient symptomology. The most common used systems are based on Seddon's classification with three broad categories: (1) neuropraxia, which does not involve loss of nerve continuity and causes only transient functional loss. (2) Axonotmesis, a complete interruption of the nerve axon and myelin while the surrounding mesenchymal structures including the perineurium and epineurium are preserved. (3) Neurotmesis, includes complete functional loss and recovery without surgical intervention does not usually occur [5], [6].

1.2 Anatomy

PNs consist of motor, sensory, and autonomic fibers, whose structural characteristics are closely related to their functional demands. For instance, conduction velocity is influenced by axon diameter and myelination, with larger, myelinated axons facilitating faster signal propagation [7].

Each neuron comprises a cell body (soma), dendrites, a single axon, and synaptic terminals. The soma is located in different anatomical regions depending on the neuron type: dorsal root ganglia (sensory neurons), autonomic ganglia (autonomic neurons), and the ventral horn of the spinal cord (motor neurons) [8]. The axons of these neurons extend peripherally and are bundled together to form nerves. These bundles are organized and protected by three distinct layers of connective sheaths: endoneurium, perineurium, and epineurium [9]. The endoneurium surrounds individual nerve fibers (axons with their associated Schwann cells), and contains endoneurial fluid, a medium similar to cerebrospinal fluid. The endoneurium consists of

fibroblasts, type 1 and 2 collagen fibrils, mast cells, macrophages, elastic fibers, and reticulin fibers. The perineurium encases fascicles (bundles of axons) and forms a selective barrier, protecting against toxins, pathogens, infections, and sudden ion fluxes [10]. The epineurium is the outermost layer that provides mechanical protection. It contains collagen fibers, blood vessels, and lymphatics.

Myelination is a process where Schwann cells (SCs) wrap their plasma membrane multiple times around an axon forming a myelin sheath. This fatty insulating layer enables saltatory conduction, where electrical impulses jump between nodes of Ranvier, gaps in the myelin sheath densely distributed with ion channels, thus significantly increasing conduction velocity compared to unmyelinated axons [7]. The axonal segments surrounded by myelin are also known as internodes [11]. Myelin is rich in a mixed group of lipids (70-80%), like cholesterol, phospholipids, galactolipids, and plasmalogens, and contain specific proteins (20-30%), including myelin protein zero (P0), peripheral myelin protein 22 (PMP22), myelin basic protein (MBP), and the myelin-associated glycoprotein (MAG) [7], [12].

In contrast, unmyelinated axons are grouped together by a single non-myelinating SC, forming structures known as Remak bundles. These non-myelinating SC (also called Remak cells) lack myelin-associated proteins such as MAG but express markers like glial fibrillary acidic protein (GFAP), vimentin, S-100, and basal membrane-associated molecules [13].

1.3 PN degeneration and regeneration

PNIs initiate a cascade of degenerative and regenerative responses in both the neuronal body and the peripheral nerve environment, including the proximal stump, the injury gap, and the distal stump [14].

Upon complete transection, the neuronal soma transitions from a neurotransmission-functional state to a regenerative state [11]. This shift involves enlargement of the cell body and dendritic retraction, accompanied by downregulation of neurotransmitter related genes and upregulation of growth associated proteins and cytoskeletal elements.

Retrograde degeneration occurs in the proximal axons, extending several millimeters back from the lesion site, while the distal axon undergoes Wallerian degeneration [11], [15]. This process begins within hours of injury and involves fragmentation of the axon and disintegration of the myelin sheath [5].

SCs play a central role in this degenerative phase. They enlarge, proliferate, and dedifferentiate, expressing regeneration associated genes such as Gap-43, various cytokines, neurotrophic factors, and the transcription factor c-Jun, which is essential for their conversion into a repair phenotype [16], [17], [18]. Together with infiltrating macrophages, SCs phagocytose axonal and myelin debris [14], [19].

As regeneration begins, SCs align longitudinally to form bands of Büngner, which act as scaffolds for regenerating axons and secrete guidance cues and trophic support [17], [18], [19]. However, in cases of severe injury or prolonged denervation, axonal sprouts may deviate from their original trajectory and mis-innervate unintended targets [5], [16].

Once regenerating axons reach their distal targets, the regenerative environment is cleared of debris and reorganized. A transient phase of excessive axonal sprouting often leads to a higher number of fibers distally than proximally [19]. Over time, these axons enlarge, mature, and remyelinate, eventually forming new fascicles enclosed by newly formed perineurium[19], [20].

1.4 Surgical repair approaches and nerve conduits

Surgical outcomes after PNI depend not only on intrinsic factors such as injury type, proximity of the lesion to target organs, apoptosis, and patients age, but also on extrinsic factors like treatment strategy, pre-and postoperative rehabilitation, and patient compliance influence. Among these, treatment strategy remains the most modifiable factor and therefore plays a crucial role in functional recovery [21].

In clinical practice, motor function restoration is prioritized over sensory recovery because it plays a more crucial role in maintaining autonomy and performing essential daily tasks. Treatment planning for nerve injuries requires careful consideration of several parameters, including the extent and type of lesion (partial or complete transection), availability of donor nerves, location of the injury, and time elapsed since trauma. For clean transections, tension-free direct coaptation via microsurgical epineural suturing or tissue glue (for small nerves) is preferred. However, in the case of large nerve gaps where direct repair would result in excessive tension, alternative bridging strategies become necessary [22]. The gold standard in such cases remains the autologous nerve transplant (ANT), typically using sensory nerves due to lower donor site morbidity. Although Wallerian degeneration still occurs within the transplanted nerve, the preserved extracellular matrix and viable SCs provide a critical scaffold for

regeneration. The main limitations of ANT are limited donor nerve availability and risk of donor site complications, including sensory loss and neuroma formation [22]. These drawbacks have led to the search of alternative strategies such as nerve allografts and tissue-engineered conduits. Processed nerve allografts, which retain the extracellular matrix but lack immunogenic cellular components, mimic ANT architecture and have shown success in bridging short gaps, though efficacy in long-gap repair remains limited [23].

Alternatively, tissue-engineered conduits made from biodegradable natural polymers or non-biodegradable and biodegradable synthetic polymers are being utilized. The U.S. Food and Drug Administration (FDA) has approved several nerve conduits for clinical use, including those composed of natural polymers such as collagen and chitosan, as well as synthetic polymers like polyvinyl alcohol (PVA) and polyglycolic acid (PGA). These conduits exhibit degradation periods ranging from 3 to 48 months. They are designed to be non-cytotoxic, non-irritating, and to possess favorable physical properties. However, despite these advantages, many of these conduits fail to support complete recovery, particularly in cases involving large nerve defects [24].

Among conduits, the muscle filled-in vein conduit (MVC) has attracted attention. This construct uses a segment of vein filled with skeletal muscle to prevent collapse, guide axonal growth, and promote SC migration. MVCs provide a bioactive environment enriched in neurotrophic factors such as nerve growth factor (NGF) and brain derived-neurotrophic factor (BDNF), supporting SC proliferation and axonal guidance [25], [26], [27], [28]. Despite these advantages, MVCs often underperform compared to ANT particularly in long-gap reconstructions [29]. The major limitation of such conduits is the lack of viable SCs, which are essential for successful regeneration.

To overcome this, cell-based therapies have been explored, using stem cells such as bone marrow-derived, adipose-derived, neural, umbilical cord, and epithelial stem cells. These therapies have shown regenerative potential but face challenges including poor survival after engraftment, risk of tumorigenesis, immune rejection, vascular complication, and ethical concerns [30], [31]. A promising alternative involves the use of extracellular vesicles (EVs) derived from stem cells. EVs from adipose-derived stem cells (ASCs) are nanoscale vesicles secreted by cells that carry neurotrophic factors, proteins, lipids, and nucleic acids which can enhance axonal elongation, modulate immune responses, and activate resident SCs after PNI [32], [33]. A drawback of EVs is the binding non-specificity, where a significant number of the injected EVs are taken up by non-targeted, healthy cells [34]. To enhance the targeting of the

EVs, minimal modification of surface markers can increase the reactivity with the target antigen. In the case of PNI, laminin can be targeted which is upregulated by SCs when they differentiate into the pro-regenerative repair phenotype. Due to this enhanced affinity to laminin, these recombinant EVs are proposed to home to the site of nerve injury following intravenous administration, enhancing the EV uptake and consequently promoting the regenerative process.

1.5 Experimental models in PNI research

To test biomaterial and surgical techniques before bringing it to a clinical setting, conduits and treatments must be tested in-vitro and in-vivo. For in-vivo testing, different animals have been used, with the rat sciatic model being the most common.

The mouse model is an attractive model for studying PN regeneration specifically to investigate relevant genes through transgenic knock-out, mutation or overexpression [35]. Mice are cheap, simple to handle and care for, and allow therefore for large study groups. Their size, however, is a limitation, as their nerves are small and complex surgeries, such those involving large defects, require great microsurgical skills. Due to this size limitation and functional testing in rats being easier, the rat model is more commonly used for in-vivo work for PN regeneration. The handling of rats is relatively similar to that of the mice, by being economically favorable. The use of transgenic rats is less available than mouse models, however due to the popularity of the rat model, functional tests for sensory and motor recovery are more standardized [36]. The translation of data obtained from rodent work to humans needs to be evaluated carefully, due to differences in nerve and gap lengths, rats exhibiting faster axonal regeneration rates, and generally better regeneration [37]. By only testing conduits on single animals models like the sciatic nerve rat model, skewed results could be obtained leading to inaccurate assessment of risks and benefits for human applications [37].

Larger defects can be studied in alternative animal models like the rabbit, sheep and monkey, the use of these animals however raises ethical concerns and generally require more care and collaboration as standardized assessment methods have not yet been established [35].

In the rat model, the sciatic nerve is the most investigated nerve, this popularity resulted in well-established protocols and assessment methods but also comes with limitations. One of these limitations is the site of the sciatic nerve being more protected against mechanical forces such as bending and tension, this allows for investigations with a clearer overview of the mechanisms

at hand but does not represent the most realistic clinical situation [37]. Additionally, the sciatic nerve transection model comes with ethical concerns. The injury causes paralysis and sensation loss of the hind limb; it is associated with auto-mutilation behavior. This causes the animal a great amount of distress and it causes an increased burden in animal care [38], [39]. Alternatively, a forelimb model such as the median nerve can be used that shows improvements regarding the ethical concerns related to the sciatic nerve model. The median nerve model only partially impairs upper limb function as specific sensory and motor functions are preserved through the ulnar and radial nerve. The rat forelimb anatomy and brachial plexus closely resemble to the human brachial plexus. Considering that upper limb injuries are most prevalent in PNI, the median nerve relates more to the clinical situation [40]. A drawback is the nerve size limitation, where the sciatic nerve allows for greater nerve gaps, that are more relevant for the human clinics.

1.6 Methods to assess PN regeneration

To evaluate PNI regeneration, several testing methods are used. In-vitro assessment is done to assess toxicity and biocompatibility before they can move to the in-vivo stage and to limit animal use [40], [41], [42]. In-vivo assessment for rodents is well established with methods assessing motoric and sensory reinnervation combined with electrophysiological conduction experiments and histology.

Sensory function is tested with the von Frey Filament test or Hargreaves test. The von Frey Filament test works on the principle of the pain response against mechanical stimuli and is used in mice and rat models. The animal is placed on a grid after which plastic pre-calibrated filaments are applied to the plantar surface of the paw. By using filaments with different stiffnesses the threshold can be determined that causes a paw withdrawal response [43]. The Hargreaves test measures the nociceptive response to heat and works along the principle of placing animals in a clear box on a glass surface. Underneath the glass surface, specifically underneath the hind paw a controlled heat beam is placed. A timer is started and the time until withdrawal is measured [44].

Motoric function can be assessed through several methods such as walking track analysis (e.g., CatWalk), staircase test, grasping test, and muscle weight ratios. The CatWalk system is a computerize gait analysis method that assesses locomotor function. Animals voluntarily cross a specialized glass walkway, where their paw contacts are illuminated by green light and

recorded by a camera. It gives parameters that allow for the evaluation of injury-related changes [45], [46]. The staircase test assesses the independent use of forelimbs in reaching and grasping tasks. Food pellets are placed on the staircase and are presented at different stages with different difficulties of reaching. The animals need to be food deprived and require training before surgery to obtain useful data [35], [43]. In the grasping test animals are lifted by their tail and grasp a grid that is connected to an electronic balance. The rats are lifted with increasing firmness until they lose their grip, after which the negative value on the balance is noted. The grasping test is a valuable test done regularly during the process of regeneration as it gives an indication on the recovery process over time [47], [48]. Lastly muscle weight ratios are often taken as a direct measure of atrophy upon injury. Values are then compared with the contralateral side or with healthy controls [36], [49], [50], [51].

Electrophysiology is a widely used method for assessing motor axon regeneration and muscle reinnervation. It is commonly employed to diagnose nerve-related conditions and evaluate regeneration after injury [26], [39]. The compound muscle action potential (CMAP) is particularly valuable for assessing motor nerve function. Several CMAP parameters are of interest in the evaluation of nerve injury and regeneration, including latency, duration, amplitude, and area under the curve (Fig. 1) [13]. The CMAP represents the summation of individual motor unit's action potentials [13]. The latency is measured in milliseconds and is described as the time elapsed between stimulation and the first deflection of the baseline, reflecting the fastest conducting axons [38]. It encompasses the time required for the stimulus to travel along the nerve, the neuromuscular junction delay, and muscle fiber signal transmission.

The duration is the measure of the entire CMAP and reflects the homogeneity of the degree of myelination of the motor axons in the nerve. The duration is either taken as negative duration from the first deflection of the baseline (2) until the end of the negative peak (4), or as total duration from the first deflection of the baseline (2) until recovery to the baseline at the end of the CMAP (6) (Fig. 1). The CMAP amplitude is proportional to the number of conducting motor axons in the nerve. CMAP amplitude may be influenced by the number of motor units responding, the stimulus, the varying conduction velocities of the axons, and the increase in motor size due to motor reinnervation. The CMAP amplitude is often taken as peak-to-peak which is taken from the negative peak (3) to the positive peak (5). Alternatively, the CMAP

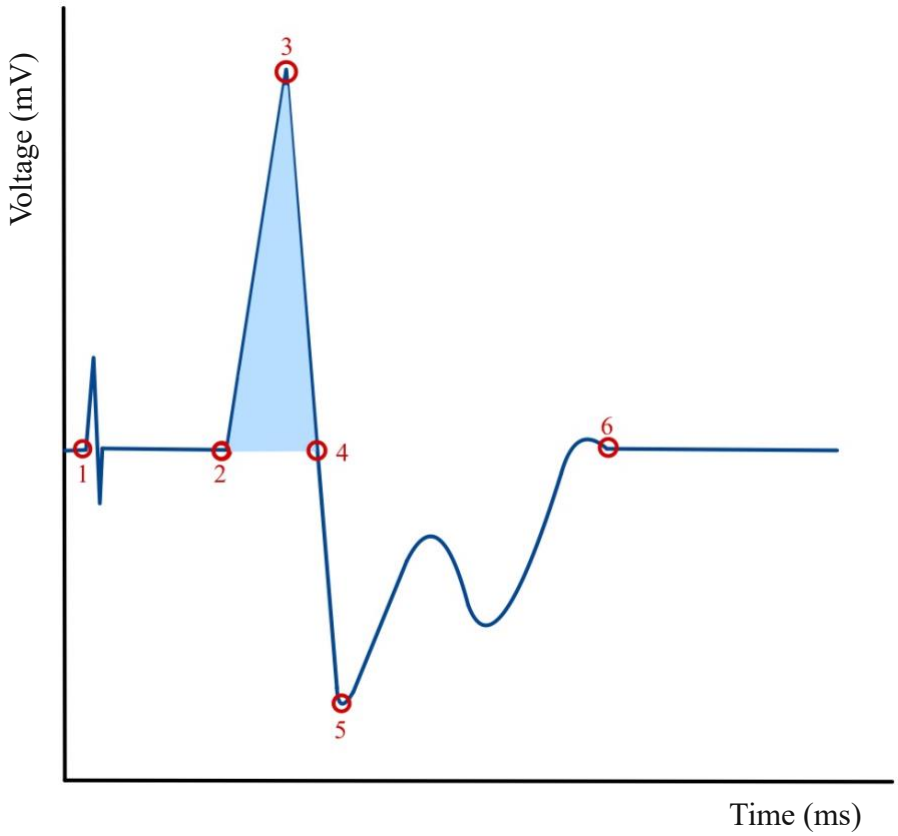

Fig.1. The compound muscle action potential (CMAP). The CMAP has several characteristics: latency, duration, amplitude, and area under the curve. The latency is taking from the point of stimulation (1) until the first deflection of the baseline (2). The negative duration is taken from the first deflection of the baseline (2) until the end of the negative peak (4). The negative amplitude is from baseline (2) to negative peak (3). The peak-to-peak amplitude is from the negative peak (3) until the positive peak (5). The negative area under the curve is represented by the light blue are of the negative peak. The total duration is from the first deflection (2) until the recovery to baseline (6).

negative amplitude can be taken which is measured from the baseline (2) to the negative peak (3) (Fig. 1). The CMAP area under the curve is most accurate for reflecting the number of myelinated axons and is often compared with histomorphometry. The area under the curve is often taken as the area of the negative peak, marked by a light blue area in Fig. 1.

Regarding histological analysis, there are several histological, immunohistochemical, and ultrastructural methods with specific applications for assessing tissue morphology, cellular phenotypes, protein expression, and subcellular structures, respectively. Hematoxylin and eosin (H&E) staining is most commonly used to stain tissues for light microscopy. Hematoxylin labels nuclei blue and eosin is detectable as a pink stain in cell cytoplasm. It is the most used staining in pathology and research using light microscopy, but not an adequate method for nerve staining because the myelin sheaths are not labeled and they are thus difficult to be detected [52], [53]. Masson's trichrome staining is a common trichrome method in muscle histology and is not often used for histological analysis of peripheral nerves. The quality of the staining is better than H&E but does not stain myelin accurately. Pre-embedding the tissue in Osmium tetroxide (OsO_4) allows for high accuracy in identifying myelin in light microscopy [54]. Schwann cells (SC) can be detected with specific glial markers, like glial fibrillary acidic protein (GFAP) and S100. To specifically stain myelinated axons, staining can be used that specifically stains the myelin sheath like: MCOLL, P0, MBP, MAG, and toluidine blue. Non-myelinated axons are associated with Remak cells that can be visualized with immunostaining, staining for p75, S100, and GFAP stains [11]. C-Jun is greatly upregulated upon nerve injury and plays an important role in the regeneration process, it is downregulated upon myelination [55]. The staining of this transcriptional factor can indicate the stage of regeneration and is believed to not show any activity after myelination is complete. Alternatively to light microscopy, nerve regeneration is assessed by Semithin and Transmission Electron Microscopy (TEM) [11]. The preparation requires effective nerve tissue fixation, and myelin preservation achieved with OsO_4 fixation. After Toluidine blue staining, tissues can be imaged and analyzed with histomorphometrically analysis, in which the number of fibers, fiber density, and fiber diameters are assessed.

Histomorphometry is a quantitative histological technique employed to evaluate structural changes and regeneration outcomes in peripheral nerves. It provides detailed morphometric data such as axon count, axon diameter, fiber diameter, myelin thickness, g-ratio (axon diameter/fiber diameter), and fiber density. These analyses are typically performed on transverse sections of nerve tissue stained with agents such as toluidine blue or osmium

tetroxide, allowing for high-resolution imaging of myelinated fibers under light or electron microscopy. The analysis can be performed using manual, semi-automatic or fully automatic methods. Fully automatic methods are increasingly supported by machine learning algorithms, enabling high-throughput processing and objective quantification [56].

Each method has distinct strengths and limitations and becomes more valuable when used in combination with the others, offering a comprehensive understanding of nerve regeneration [57].

1.7 Aim of this thesis

This thesis investigates the regenerative potential of extracellular vesicles (EVs) derived from adipose-derived stem cells, with modifications to enhance their laminin-binding, in the context of peripheral nerve repair over gap defects. Current clinical strategies show superior regenerative outcomes with autologous nerve transplants compared to more accessible nerve conduits. However, the limited availability and associated donor site morbidity of ANTs necessitate the development of effective alternatives, such as synthetic or biologically derived nerve guidance conduits.

In this study, a delayed repair model of the rat median nerve with a 7 mm gap was employed to simulate clinical scenarios in which immediate nerve repair is not feasible. A muscle filled-in vein conduit was evaluated as an alternative to the autologous nerve transplant, with both repair strategies receiving either wildtype or laminin-binding enhanced EVs. The primary objective was to determine whether EV treatment could improve regeneration outcomes in the muscle filled-in vein conduit to a level comparable with the autologous nerve transplant.

Additionally, this thesis explores a novel and cost-effective approach to histomorphometric analysis by employing AxonDeepSeg (ADS), an automated segmentation tool, in combination with myelin basic protein (MBP) immunostaining. It is hypothesized that this method enables reliable automated quantification of myelin and axonal structures, with morphometric data that meaningfully correlates with electrophysiological outcomes.

2 Methods

2.1 Animals

48 male Lewis rats with an average weight of 484g (432-522g), underwent surgery to remove 7-mm of the right median nerve. After this transection, the right flexor digitorum superficialis (FDS) muscle, normally innervated by the median nerve, began to lose mass (Fig. 2a). After 8 weeks, the left median nerve was removed and transplanted onto the right arm for half of the animals (*n*=24) (Fig. 2b-c). The other 24 animals received a muscle filled-in vein conduit constructed from the left gracilis muscle and left epigastric superficialis vein to be transplanted unto the right median nerve gap. This conduit is fabricated by pulling the vein tissue over the muscle tissue creating a tube-like structure. The left median nerve was also removed in the MVC group, resulting in all animals portraying denervation in the left FDS muscle. Additional to the conduit, the animals received ASC derived EV therapies: wildtype, modified EVs with increased laminin-binding properties, and a PBS vehicle control (Fig. 1d). In the conduit groups (*n*=48, MVC: *n*=24, ANT: *n*=24), rats were evenly assigned to three EV treatment conditions, 8 received wild-type EVs (5×10^8 /20 µL), 8 received modified EVs (5×10^8 /20 µL), and 8 animals received PBS as a control treatment (Table 1). Following a 12-week recovery period, the animals were assessed to compare two types of conduits: autologous nerve transplant and muscle filled-in vein conduit. Weight data from a separate study, in which the rats were

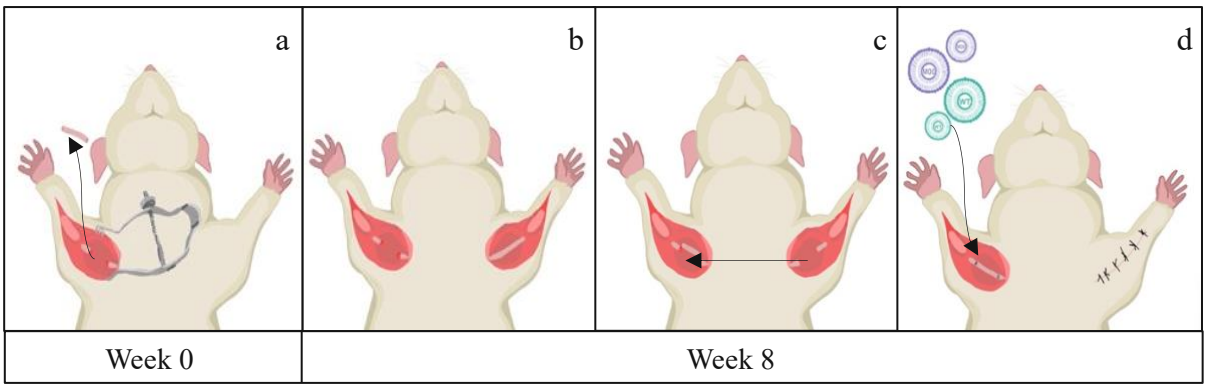

Fig. 2. Illustrative description of autologous nerve transplant, median nerve surgery and EV treatment. (a) Right median nerve excision. (b) after 8 weeks the left side is opened and (c) median nerve is excised and transplanted to the right injury site. (d) Left median nerve is fixed with sutures to the distal and proximal native ends, EV treatment is injected intraneural (either modified, wildtype or control).

monitored until sacrifice, was used to assess whether all animals and groups in this study followed normal growth patterns.

Table 1: Distribution of animals according to their surgical treatment

Treatment	Number of animals
Autologous nerve transplant with wildtype EVs	7
Autologous nerve transplant with modified EVs	8
Autologous nerve transplant with control vehicle	7
Muscle filled-in vein conduit wildtype EVs	7
Muscle filled-in vein conduit with modified EVs	8
Muscle filled-in vein conduit with control vehicle	7

2.2 Electrophysiology

Electrophysiology is performed to measure CMAPs, which reflect the functional reinnervation of muscles and the efficacy of nerve regeneration. The experiment was performed at the end of the 12-week recovery period, for which the animals first were anesthetized. The rat was placed in the supine position and the limbs were taped to the surgery table to ensure stability and immobilization during the procedure. Underneath the rat, a heating pad was placed to maintain the rats body temperature. The right arm was surgically opened and held open with surgical retractors. Then the median nerve was dissected free of surrounding tissues. A sterile plastic was placed underneath the nerve and between the electrode and surrounding tissues to prevent noise. During this procedure 4 animals were observed to have ruptured median nerves and were therefore excluded from the study.

The electrode placement was done microscopically. A bipolar stimulating electrode was positioned with a micromanipulator distal and proximal to the repaired nerve segment, slightly beyond the respective suture points. The active electrode was placed in the right flexor digitorum superficialis muscle, and the reference electrode in the second digit. A ground electrode was placed in the right hind limb (Fig. 3) (Natus® Ultra Disposable Subdermal Needle Electrodes). For the measurements, the software-controlled electrical stimulation and electromyogram recording device (Keypoint® Focus EMG / NCS / EP System) was connected to a notebook computer. The Keypoint software was used in the configuration of motor nerve conduction specifically for the median nerve. This setup measured the CMAP latency, duration, amplitude, and area under the curve. The exact parameters measured were the latency, total duration, peak-to-peak amplitude, and area under the curve as described by Fig. 1.

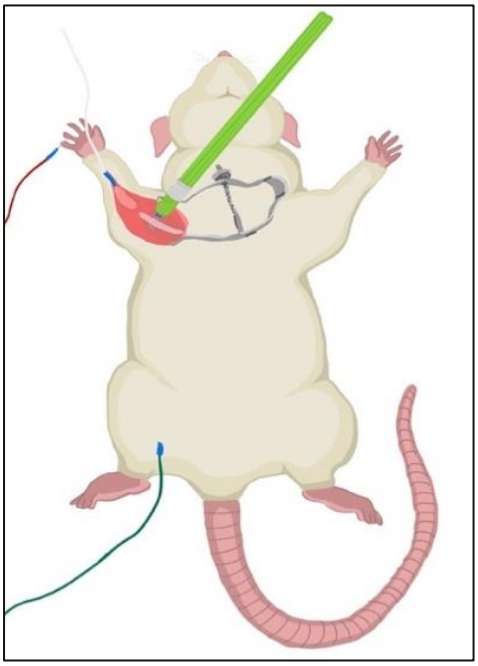

Fig. 3. Illustrative description of electrophysiology set up

Prior to measurement, the rectal temperature was recorded as a control, since temperature affects electrophysiology [58]. Then surrounding electrical equipment was turned off during the measurements to minimize interference. Current stimulation was applied from 0 to 1.5 mA in 0.1 mA increments and extended up to 2.0 mA to reach supramaximal stimulation. The experiment was performed on both the distal and proximal sites of the nerve transplant, past the sutures.

2.3 Histology

2.3.1 Sample preparation

After the electrophysiological measurements, the animals were sacrificed after which a segment of the right median nerve containing the reconstructed nerve segment was excised as well as both left and right FDS muscle. For histological evaluation, harvested regenerated right median nerves and both FDS muscles of all animals were subjected to staining and evaluation. The FDS muscles were immediately weighed to obtain the wet muscle weight, photographed and measured on millimeter paper (Fig. 4). After this, all tissues were fixed for 24h in paraformaldehyde, followed by 1h of washing in flowing water, dehydration for 1h at 50%

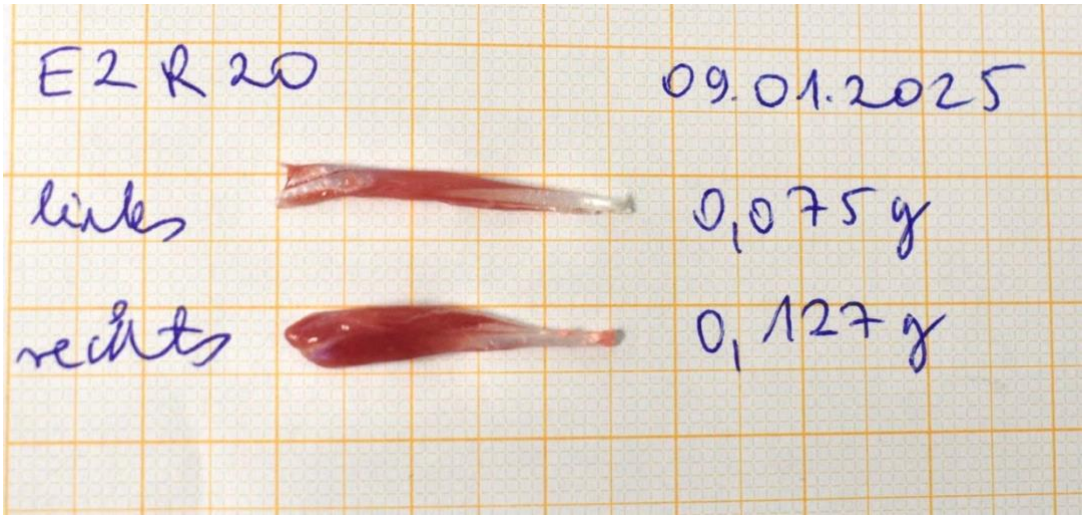

Fig. 4. Freshly harvested FDS muscles weighed and photographed on millimeter paper. Representative image from animal No. 20 from the ANT + modEVs groups

ethanol and then stored in 70% ethanol. Further histological preparation was performed by the histology team who embedded the samples in paraffin, cut the samples in transverse direction on a microtome in 4 µm sections, and placed them on glass slides. For the median nerves 4 slices were stained per nerve, cut at a location proximal, proximal to the middle, distal to the middle and distal to the sutures (Fig. 5). The proximal (cut 1) and distal (cut 4) locations match the electrophysiology stimulation locations.

2.3.1 H&E staining

Hematoxylin and Eosin (H&E) staining was performed to assess overall tissue morphology and detect structural changes such as degeneration, inflammation, or regeneration. The staining was performed by the team of histology on the right median nerve segment with a standard H&E staining protocol.

2.3.2 Immunohistochemistry (IHC)

Immunohistochemical staining was performed on the right median nerve segments to evaluate key cellular responses involved in PN regeneration. Three markers were selected to target specific aspects of SC behavior and myelin integrity. C-Jun staining was used to identify activated SCs engaged in the regenerative response, as c-Jun is a transcription factor upregulated in the repair phenotype of SCs. Its nuclear localization allows identification of c-Jun positive cells by brown nuclear staining, while all nuclei are counterstained blue with hematoxylin. GFAP staining was performed to detect non-myelinating SCs, providing insight

into the glial response to injury. GFAP-positive structures appear brown against a blue nuclear counterstain. Finally, myelin basic protein (MBP) staining was used to visualize the extent of myelination, enabling assessment of demyelination and remyelination in the regenerating nerve. MBP staining served as the structural basis for subsequent histomorphometric analysis. All immunostaining was performed by the histology team, with MBP staining conducted both with and without hematoxylin counterstain to support imaging and segmentation needs.

2.3.3 IHC protocol

Immunohistochemical staining was performed on paraffin-embedded sections of the right median nerve to evaluate cellular markers involved in peripheral nerve regeneration. Slides were first deparaffined and rehydrated through a graded ethanol series into distilled water. Antigen retrieval was performed using heat induced epitope retrieval (HIER): sections were placed in EDTA buffer (pH9) and heated for 20 minutes, followed by steaming in the same hot buffer for 20 minutes. After retrieval, slides cooled down for approximately 30 minutes before being transferred to a humidified chamber for staining.

To block endogenous peroxidase and alkaline phosphatase activity, sections were incubated for 10 min with BLOXALL® dual enzyme blocking solution (Vector Laboratories, SP-6000). Following this, the sections were incubated for 1 hour with the following primary antibodies: (i) rabbit anti-c-Jun antibody (Abcam, ab40766, 1:200), (ii) rabbit anti-GFAP antibody (Millipore, AB5804, 1:1000), (iii) rabbit anti-MBP antibody (Abcam, ab133620, 1:1000). After primary antibody incubation, slides were washed three times in TBS-T and then incubated for 30 minutes with a horseradish peroxidase (HRP)-conjugated secondary antibody (BrightVision poly-HRP Anti-rabbit IgG, ImmunoLogic), ready to use. All incubation steps were followed by three times washing in TBS-T.

The slides were incubated with NovaRed substrate (Vector Laboratories, ImmPACT NovaRED®, SK4805) for 6 minutes allowing the enzymatic reaction to develop visible staining. Sections were then counterstained with hematoxylin, followed by dehydration and mounted with coverslips for microscopic evaluation.

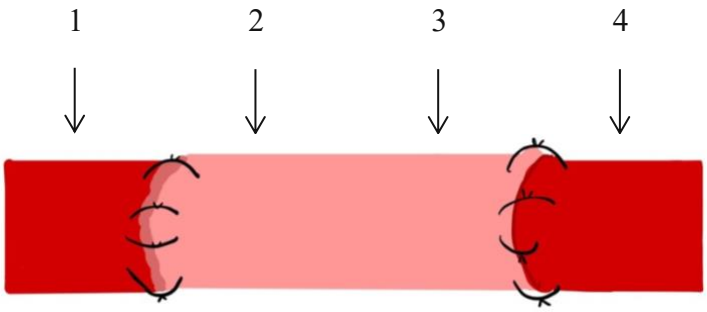

Fig 5. Schematic overview of histological cuts of median nerve. (1) proximal to graft, before sutures, (2) proximal to middle of graft, (3) distal to middle of graft, and (4) distal to graft, past the sutures.

2.3.5 MSB staining

Martius-Scarlet-Blue (MSB) staining was performed to evaluate fibrotic changes in muscle tissue by differentiating collagen, muscle fibers, and fibrin, particularly in response to denervation. The staining was performed by the team of histology on the FDS muscle sections.

Paraffin embedded tissues are first deparaffinized and rehydrated through graded alcohol into distilled water. Slides were re-fixed in Bouin's solution for 1 hour at 56ºC. Excess yellow coloration was removed by rinsing under running tap water for at least 30 minutes, with visual inspection. Nuclear staining was performed with Weigert's iron hematoxylin solutions A and B mixed 1:1) for 5 minutes. Brief dedifferentiation was performed in 0.25% hydrochloric acid in ethanol (HCl-EtOH). Sections were rinsed in running tap water for 5 minutes to allow bluing of the nuclei. Sections were stained for solution A (Martius Yellow) for 2 minutes. Rinsed in distilled water, then stained in solution B (Brilliant crystal scarlet) for 10 minutes. Washing again in distilled water, then treated with solution C (1% phosphotungstic acid) for 10 minutes, rinsed in distilled water. Then stained in solution D (Methyl blue) for 4 minutes. Briefly rinsed in solution E (1% acetic acid). Rapid dehydration with automated tissue processor. Sections are cleared in xylene for 5 minutes. To finish, slides were cover slipped.

All staining reagents used in this study were prepared in-house using analytical-grade chemicals from Sigma Aldrich, Roth, and Merck. Bouin's fluid, used for post-fixation, was freshly prepared by combining 75 mL of saturated picric acid solution (1.3%, Sigma Aldrich, P6744-

1GA, CAS 88-89-1), 25 mL of formaldehyde solution (≥37%, acid-free, Roth, P733.2, CAS 50-00-0), and 5 mL of acetic acid (100%, Roth, 3738.1, CAS 64-19-7).

For the staining protocol, 5 dye and buffer solutions (A-E) were prepared according to established histological procedures. Solution A was prepared by dissolving 0.5g of Martius Yellow (Sigma Aldrich, 377767-25G, CAS 605-69-6) and 2g of phosphotungstic acid hydrate (Sigma Aldrich, 79690-100G, CAS-12501-23-4) in 100 mL of 96% ethanol. Solution B consisted of 1g of Brilliant Crystal Scarlet (Crystal Ponceau 6R, Sigma Aldrich, C0644-5G, CAS 2766-77-0) dissolved in 100 mL distilled water, with the addition of 2 mL of acetic acid. Solution C, used for differentiation, contained 1g of phosphotungstic acid hydrate in 100 mL of distilled water. Solution D was prepared by dissolving 0.5g of methyl blue (Merck, 1163160050, CAS 28983-56-4) in 100 mL of distilled water with 1mL of acetic acid. Finally, solution E was used as a brief acidic rinse and consisted of 1mL of acetic acid in 100 mL of distilled water. All solutions were prepared fresh and stored at 4ºC in light-protected glass containers until use.

2.3.6 Bright field microscopy

All stained sections were imaged using the Olympus Slideview VS200 ASW 4.1.1 slidescanner with the 20x /0.80 objective (0.274 µm/pixel). The images were evaluated with the Olympus OlyVIA 4.2 image viewer software, in which images can be processed and converted for further analysis.

2.4 Histomorphometry of median nerve

To enable systematic and reproducible analysis of peripheral nerve morphology, a dedicated workflow for histomorphometry was developed. Particularly, this pipeline integrates immunohistochemically stained slices using MBP as a myelin sheath marker, an approach not previously adapted for automated analysis. The pipeline was developed to facilitate semi-automated segmentation and quantification of axons and myelin using AxonDeepSeg (ADS), an open-source automated segmentation software. A visual representation of this workflow is provided in Fig. 6. The analysis according to this workflow of the median nerve was performed on all histological sections from the four anatomical sites, using MBP stained histological slices without counterstain (Fig. 5).

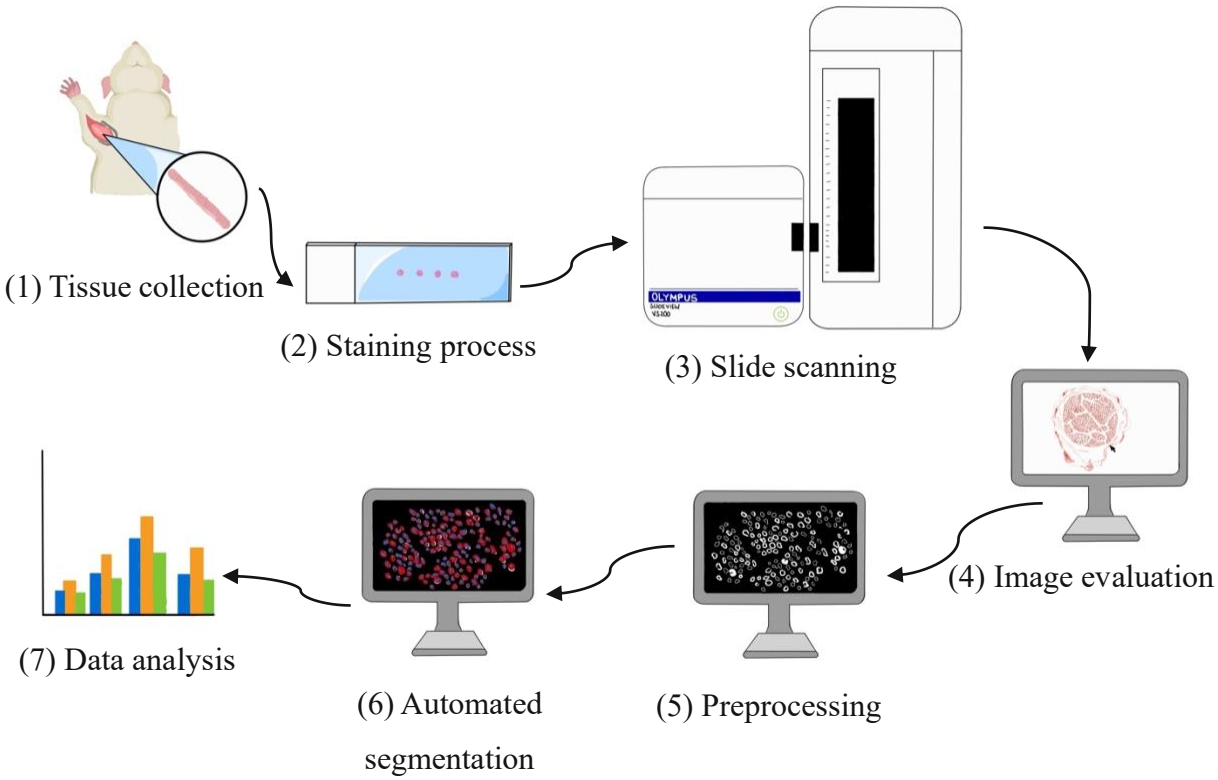

Fig. 6. Representative workflow of histomorphometry segmentation process. After the 12-week recovery period, the median nerve is harvested and processing through paraffin embedding, cutting process and slide montage. The slide is stained with specific MBP-staining procedure and images through the OLYMPUS VS200 slidescanner. The images are evaluated in OlyVIA and preprocessed in ImageJ as preparation for segmentation. In AxonDeepSeg the images are automatically segmented for axon and myelin. Then, Data analyses are performed to obtain histomorphometric results.

The established workflow includes the following steps: (1) tissue harvesting, (2) tissue preparation and previously described histological processing with MBP staining, (3) obtaining high-resolution images of the stained sections using brightfield microscopy (OLYMPUS VS200, slidescanner), (4) Qualitatively evaluate images, (5) preprocessing of image files in ImageJ, to enhance the detection of myelin structures (find a more detailed description below), (6) segmentation using ADS, (7) post-processing and quantitative analysis of axonal and myelin features through the morphometrics option of ADS.

2.4.1 Preprocessing with ImageJ

For the preprocessing, images were first split into their red, green, and blue components using the "split channels" function under the RGB color model. The red channel was closed showing the weakest MBP signal, the other channels were merged again and converted to 8-bit grayscale to enable intensity-based filtering. A Fast Fourier Transform (FFT) Bandpass Filter was then applied to remove background noise and enhance structural features, using parameters to filter large structures down to 20 pixels and filter small structures up to 1 pixel. Finally, a manual threshold was applied with a cutoff value at 115, to segment MBP positive areas.

2.4.2 Automated segmentation with AxonDeepSeg

Segmentation was performed using the open-source automatic segmentation software, AxonDeepSeg (Napari version 0.5.6) (ADS version 5.0.0) [59]. The software is designed for histomorphometric analyses based on TEM, scanning electron microscopy (SEM), or bright field images with osmium tetroxide fixation. For the analysis of MBP-stained slices, the bright field model is applied. Specifically, the software applied the model_seg_generalist_BF, which is trained on bright-field microscopy images. Using this model, ADS segmented the images to identify axons and myelin, from which histomorphometric data were extracted. To compensate for potential errors, in automatic detection, manual corrections were performed, making the method semi-automatic. This extracted histomorphometric parameters included the following [53]:

- The total cross-sectional area
- The total fiber numbers
- Fiber density
- G-ratio

- Axon diameter
- Fiber diameter
- Myelin thickness

Histograms are generated to visualize the distribution of axon and fiber diameters. Diameter values were grouped into gradual 1µm intervals, and the number of fibers per bin was counted for each animal individually. The data were subsequently grouped by anatomical level (cut 1-4) to assess regional variation in diameter distributions across the nerve.

2.5 Muscle analysis

Muscle analysis was performed through muscle weighing and fibrin area calculation to quantify muscle atrophy or preservation by comparing muscle mass of healthy muscles to the weight after nerve injury and regeneration. The FDS muscles are evaluated by comparing the muscle weight, circumferential area and fibrin percentage between the groups. The right FDS muscle underwent an 8-week denervation period (median nerve removal) followed by a 12-week reinnervation period. The left FDS muscle was left untouched for the 8-week period after which it was denervated (left median nerve segment removed) for 12 weeks. The right FDS muscle is evaluated using the ratio of right to left.

$$muscle\ ratio = \frac{FDS_{right}}{FDS_{left}}$$

Additionally the right FDS muscle is evaluated as a percentage of the average healthy FDS muscle weight obtained from 4 control animals [47].

$$weight\ percentage\ of\ healthy\ FDS\ muscle = \frac{FDS_{right} \times 100\%}{FDS_{healthy}}$$

The muscle was prepared by the histology team and stained for Martius-Scarlet-Blue (MSB). This trichrome-type staining results in red-colored fibrin and muscle tissues and blue-colored collagen and older fibrin clusters. The circumferential area of the muscles was measured in OlyVIA with the Freehand Polygon tool. Spearman's correlation was calculated for the relationship between the FDS muscle surface area and the muscle weight of the left FDS muscle using GraphPad Prism software, in which $P<0.05$ was considered statistically significant.

The fibrin area was calculated in Fiji (ImageJ). In ImageJ the plugin Colour Deconvolution was used which is useful to unmix dyes in bright field microscopical images with histology stains [60]. In this plugin the vectors were chosen for Azan-Mallory staining which give compatible

results for MSB muscle staining. From this the second color (pink) was chosen to further process. The image was converted into a grayscale 8-bit image from this the threshold was taken with the automatic thresholding function. The scale was set to match the pixel size of the images obtained from the slide scanner. Then analyze particles was used from 10 to infinity to filter out noise which ultimately gives the total "pink" area, representing fibrin/muscle tissue. Then for comparative purposes the percentage of fibrin area of total area was calculated with the following equation:

$$Fibrin\ area\ percentage\ of total\ muscle\ area\ = \frac{Area_{fibrin}\ \times\ 100\%}{Area_{total\ muscle}}$$

2.6 Data extraction and statistics

The CMAP latency, duration, amplitude, and area under the curve were extracted from each curve for each stimulus current amplitude (mA) to analyze the results. The software used for the experiments did not support raw data export, so key points of the CMAP signal, such as onset, maximum negative peak, zero crossing, maximum positive peak, and end, had to be manually selected. This was necessary to ensure consistent and comparable measurement of latency, duration, amplitude, and area under the curve across all animals and individual recordings. The parameters were determined with different approaches. CMAP amplitude and area under the curve are reaching a maximum plateau when reaching the supramaximal stimulation intensity therefore the maximum observed value is used for statistical analysis. For CMAP duration and latency, the curves reached a plateau of which the average is taken for statistical analysis. This plateau is found by plotting each animal's latency against the stimulus value (mA) from which the plateau is determined. Statistical analysis was done with GraphPad Prism software, version 10 for macOS (GraphPad Software San Diego, CA). Normality tests showed no consistent normal distribution for the investigated groups therefore the Kruskal-Wallis (non-parametric) test was done with Dunn's multiple comparisons test. $P<0.05$ was considered statistically significant.

The data of the electrophysiological measurement is compared to the histomorphometric data with a simple linear regression taking the 7 histomorphometry parameters as independent and the 4 electrophysiological as dependent [26].

3 Results

3.1 Animal weight

Body weight increased steadily over time in all animals, with no significant differences observed between experimental groups (Fig. 7). Detailed individual body weight trajectories are provided in Appendix A1.1.

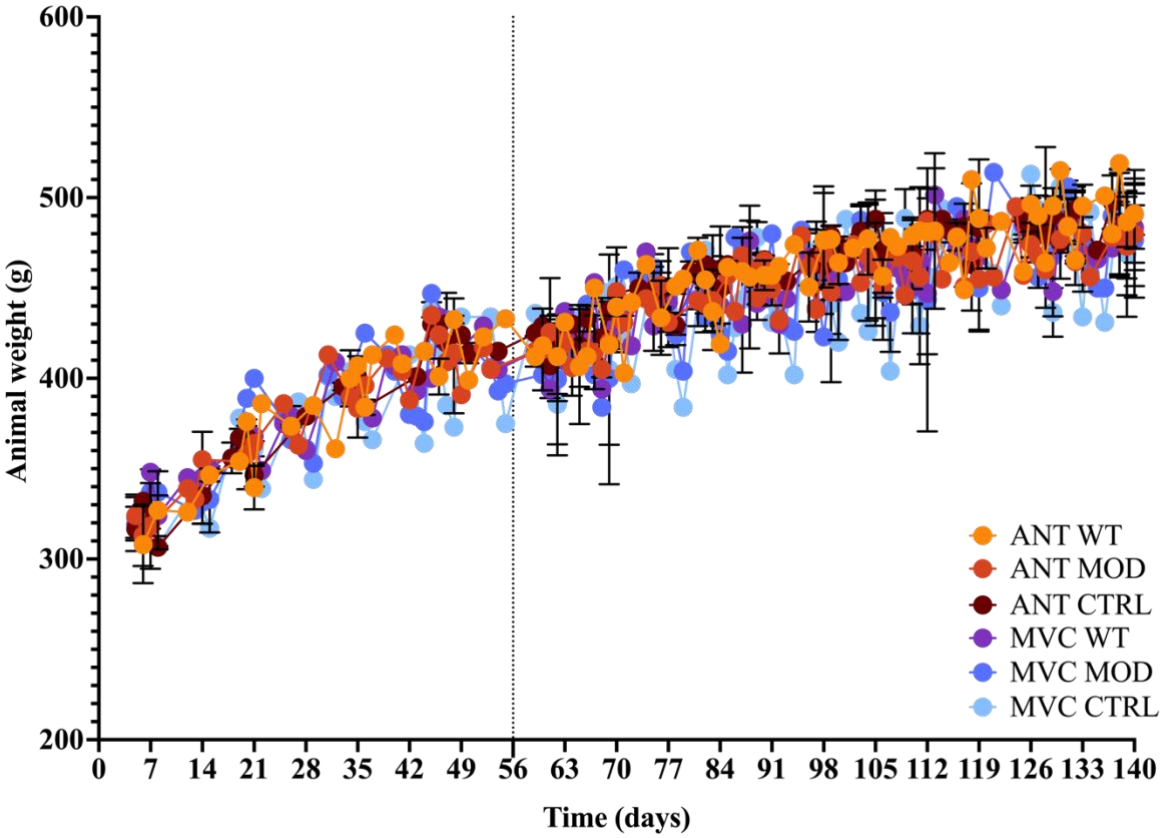

Fig. 7. Increase in body weight over time. Values represent mean ± standard deviation. The vertical line at 8 weeks indicates the time point of the secondary surgery, during which nerve repair with ANT or MVC and EV treatment was performed.

3.2 Electrophysiology

In-vivo electrophysiological assessment of the median nerve showed a significant difference between the ANT + modEV and the MVC + modEV groups, where the ANT achieved greater peak-to-peak CMAP amplitudes and area under the curve (Fig. 8). The amplitude difference reflects better muscle reinnervation for the ANT and greater area under the curve reflects a greater total muscle response for ANT than for MVC (Table 2). No significance was found for

latency and duration. Within the conduit groups no significance was found due to the large standard deviation.

Table 2: Mean and Standard Deviation of CMAP Parameters for MVC and ANT across EV treatment groups

		Wildtype EV		Modified EV		Control	
		ANT	MVC	ANT	MVC	ANT	MVC
Latency (ms)	Distal	1.51± 0.29	1.35± 0.64	1.34± 0.20	1.36± 1.83	1.48± 0.40	1.52± 1.17
	Proximal	1.29± 0.57	1.21± 0.55	1.20 ± 0.28	1.01± 1.44	1.16± 0.25	1.02± 0.75
Duration (ms)	Distal	6.43± 1.81	5.30± 2.69	6.68± 0.43	3.46± 2.99	6.17± 1.32	4.72± 3.34
	Proximal	6.04± 1.65	5.06± 2.57	6.95± 0.73	3.05± 3.50	6.19± 0.80	4.35± 2.81
Amplitude (mV)	Distal	8.70± 3.74	3.65± 4.06	11.29± 2.87 **	2.29± 3.90	11.44± 6.45	3.86± 4.75
	Proximal	9.37± 4.29	6.32± 6.06	11.10± 2.93 *	2.22± 3.88	10.00± 6.32	3.00± 4.76
Area under the curve (mV * ms)	Distal	7.12± 3.34	3.22± 4.00	8.74± 2.24**	1.81± 3.07	8.55± 5.12	2.83± 3.40
	proximal	7.32± 3.44	5.33± 5.55	9.11± 2.79*	1.88± 3.30	7.70± 5.18	2.54± 3.86

Note. EV treatment groups included modified EVs, wildtype EVs, and vehicle control. Statistical significance between MVC and ANT was assessed using the Kruskal–Wallis test followed by Dunn's post hoc test (*p<0.05, **p<0.01 between ANT and MVC).

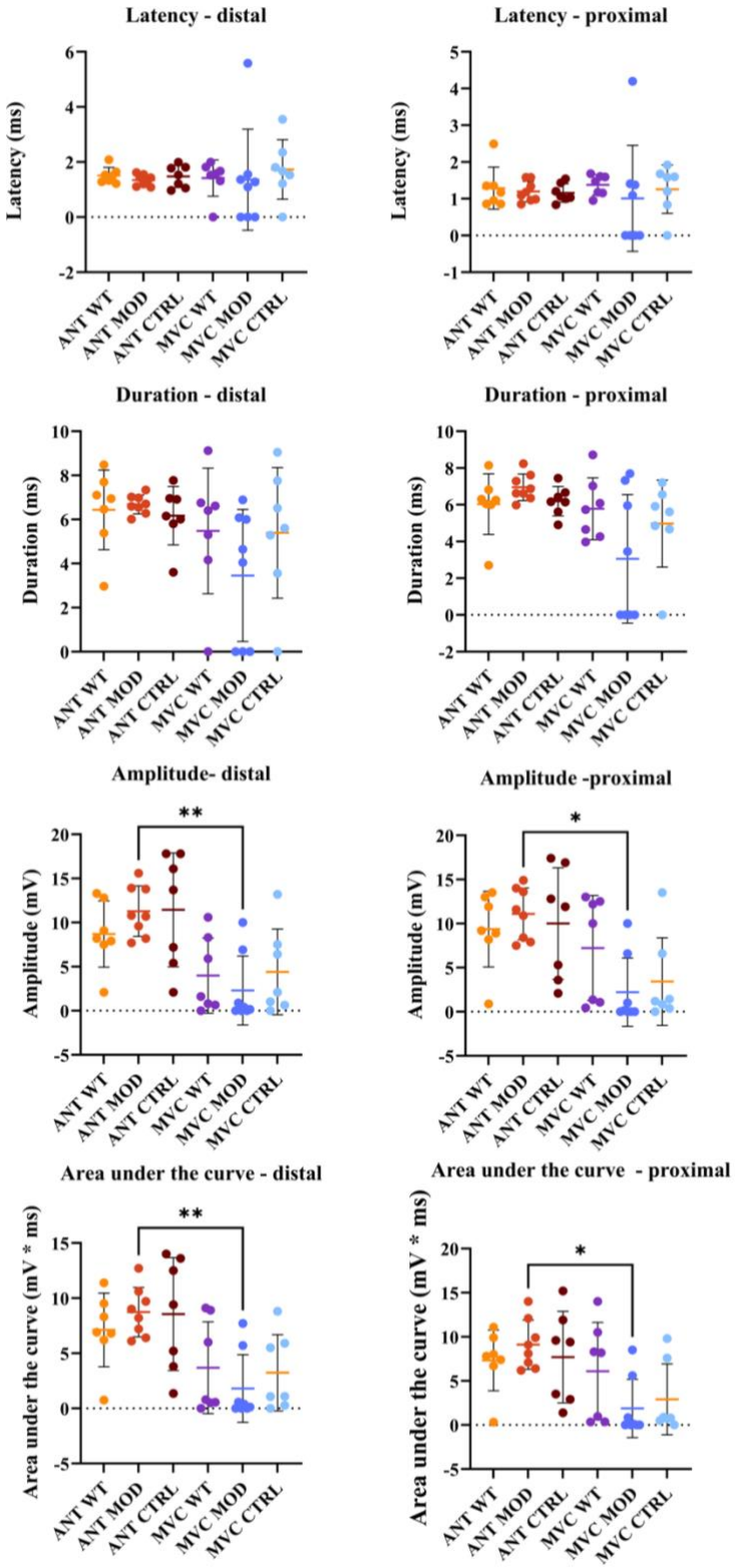

Fig. 8. Quantitative electrophysiology CMAP data. The compound muscle action potential (CMAP) parameters analyzed include (a-b) latency, (c-d) duration, (e-f) amplitude, and (g-h) area under the curve. Data are presented for 6 experimental groups, including autologous nerve transplant (n=22) and muscle filled-in vein conduit (n=24). Statistical significance was determined using ANOVA followed by the Kruskal-Wallis multiple comparison test (*p <0.05, **p<0.01).

3.3 H&E staining

Representative H&E-stained section of the ANT and MVC groups revealed distinct morphological differences in tissue structure and remodeling at the implantation site (Fig. 9). In the ANT groups, a clearly defined layer of loose connective tissue around the epineurial layer was consistently observed, especially in sections in the implant (cut 2 and 3), suggesting progressive remodeling and possible structural stabilization.

In contrast, the MVC conduit sections retained recognizable native muscle fibers within the center of the graft (anatomical levels 2 and 3). These muscle fibers often displayed a vacuolated appearance with clear, white regions within the cytoplasm. These regions are interpreted as adipose tissue, a sign of muscle fiber atrophy and degeneration, a known phenomenon during muscle tissue remodeling when not functionally reinnervated [61]. The nerve tissue mainly formed inside the vein walls, confirmed with MBP staining (Fig. 12)

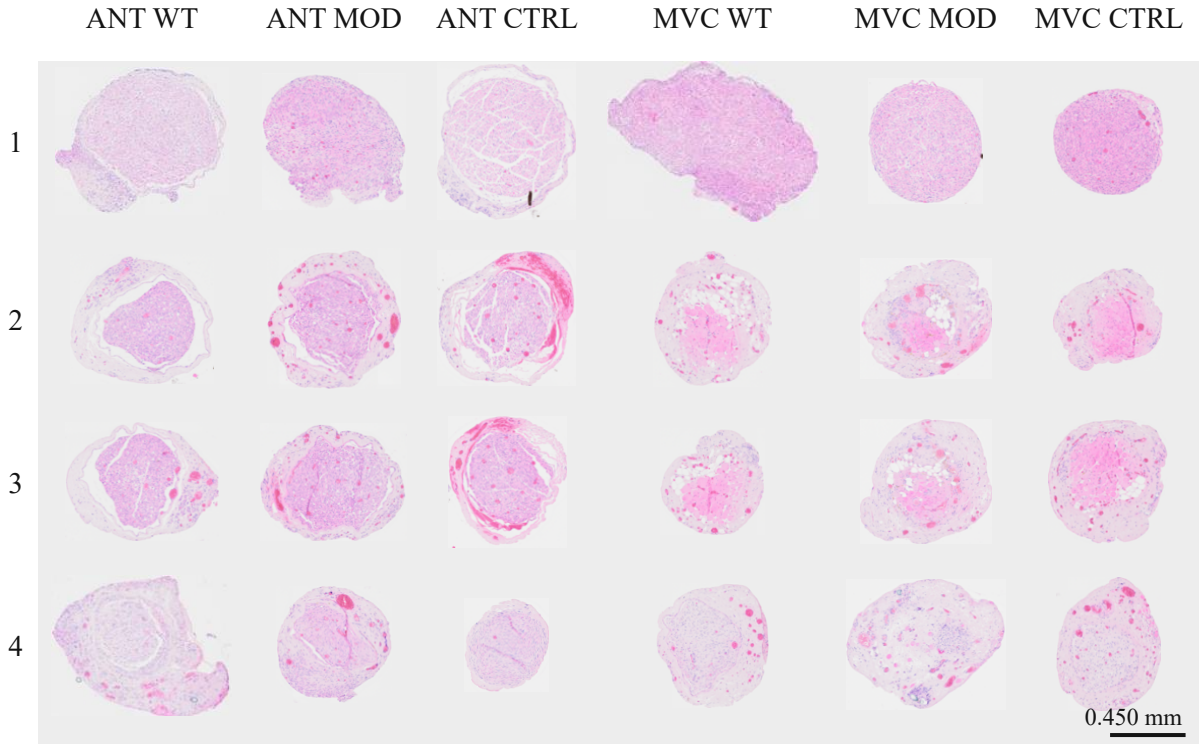

Fig. 9 H&E staining of median nerve across autologous nerve transplant (ANT) and muscle filled-in vein conduit (MVC) and extracellular vesicle treatment at four anatomical locations. Representative bright field images of 12-week regenerated nerve post 8-week delay at 4 anatomical sites: (1) proximal of implant, (2) proximal of conduit middle cut, (3) distal of conduit middle cut, and (4) distal of conduit. The origin of the images can be found in Table A1.1.

3.4 c-Jun staining

Immunostaining for c-Jun was used to assess cellular activation in response to nerve injury and regeneration, with a focus on SCs, but recognizing that c-Jun can also be expressed in other cell types such as neurons, fibroblasts, and immune cells. Strong nuclear c-Jun expression was observed throughout the nerve transplant for the ANT treated groups, indicating cellular activation, primarily attributed to SCs, but potentially also involving other reactive or regenerative cell types. In the MVC treated group, c-Jun expression within the conduit (anatomical sites 2 and 3) was limited, with higher levels detected proximal and distal to the transplant, suggesting localized activation outside the central graft (Fig. 10). The ANT group treated with modified EVs showed variable expression, with some animals exhibiting widespread c-Jun activity and others showing little to none. This may reflect differences in regenerative status, where low or absent c-Jun expression could indicate a completed resolved repair response or completed regeneration.

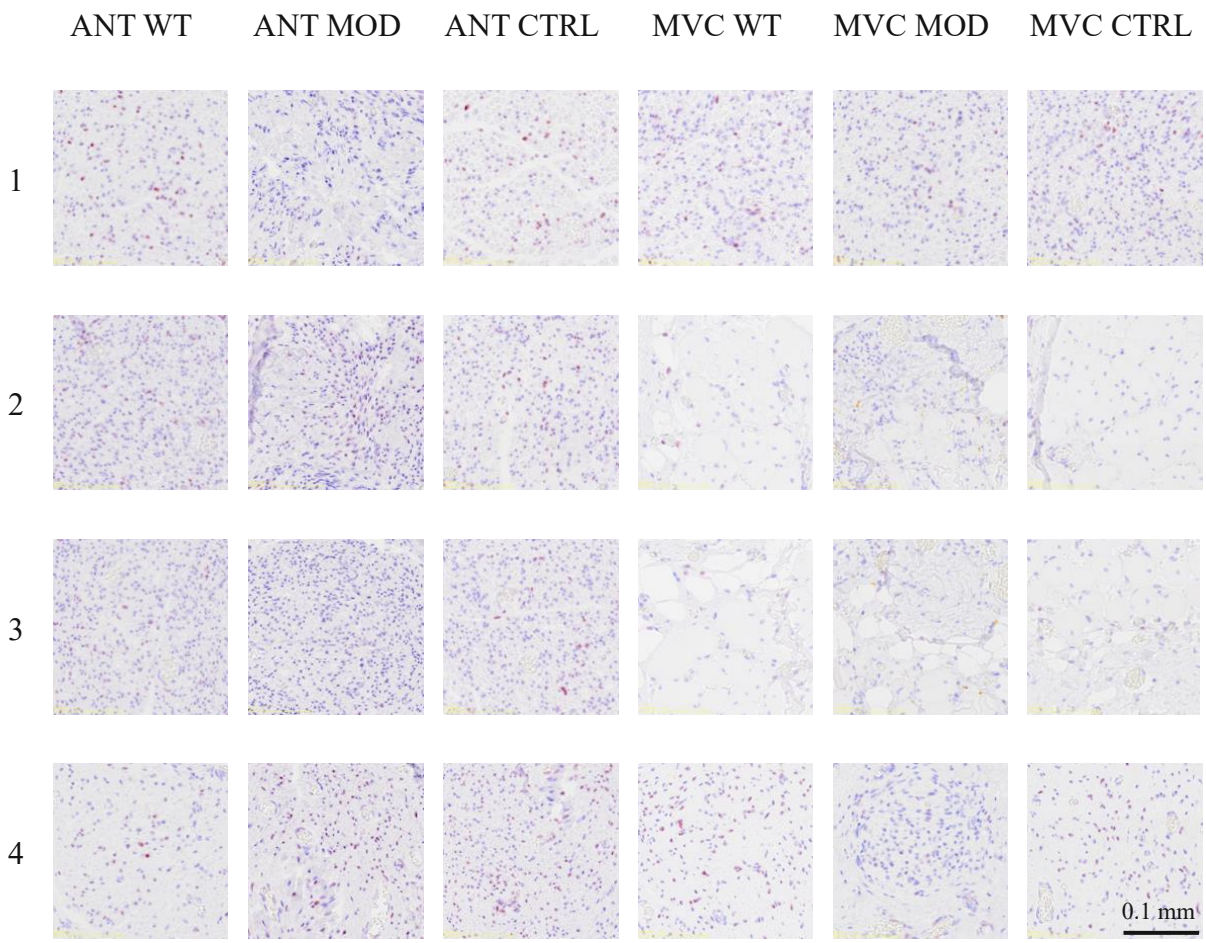

Fig. 10. c-Jun staining of central regions of histological sections from 4 median nerve sites across autologous nerve transplant (ANT) and muscle filled-in vein conduit (MVC) with extracellular vesicle treatment. Representative bright field images of regenerated nerves at 12 weeks post repair following an 8-week delay, shown at 4 anatomical sites: (1) proximal of implant, (2) proximal of conduit middle cut, (3) distal of conduit middle cut, and (4) distal of conduit. Image identifiers can be found in Table A1.1.

3.5 GFAP staining

GFAP staining revealed positive GFAP signal in the first anatomical location (cut 1) for all treatment groups, where GFAP-positive cells are found diffusively throughout the tissue (Fig. 11). The positive signal seams coherent with non-myelinating SCs in contact with axons. In the conduit cuts (cut 2 and 3) less diffusive signal is found, rather strong signals at blood vessels (ANT). In the MVC the strongest GFAP positive signal is found in the vein demonstrating different morphology than found in the proximal parts, not matching expected non-myelinating SCs relating to axons. The ANT groups display again diffusive GFAP positive signal in the

distal cut (4), likely displaying non-myelinating SCs related to non-myelinated axons, throughout the tissue. The MVC displays few diffusive GFAP signal and has strong signal in blood vessels, and connective tissues. Not all animals displayed the same intensity of signal in the outer connective tissue layers, and blood vessels.

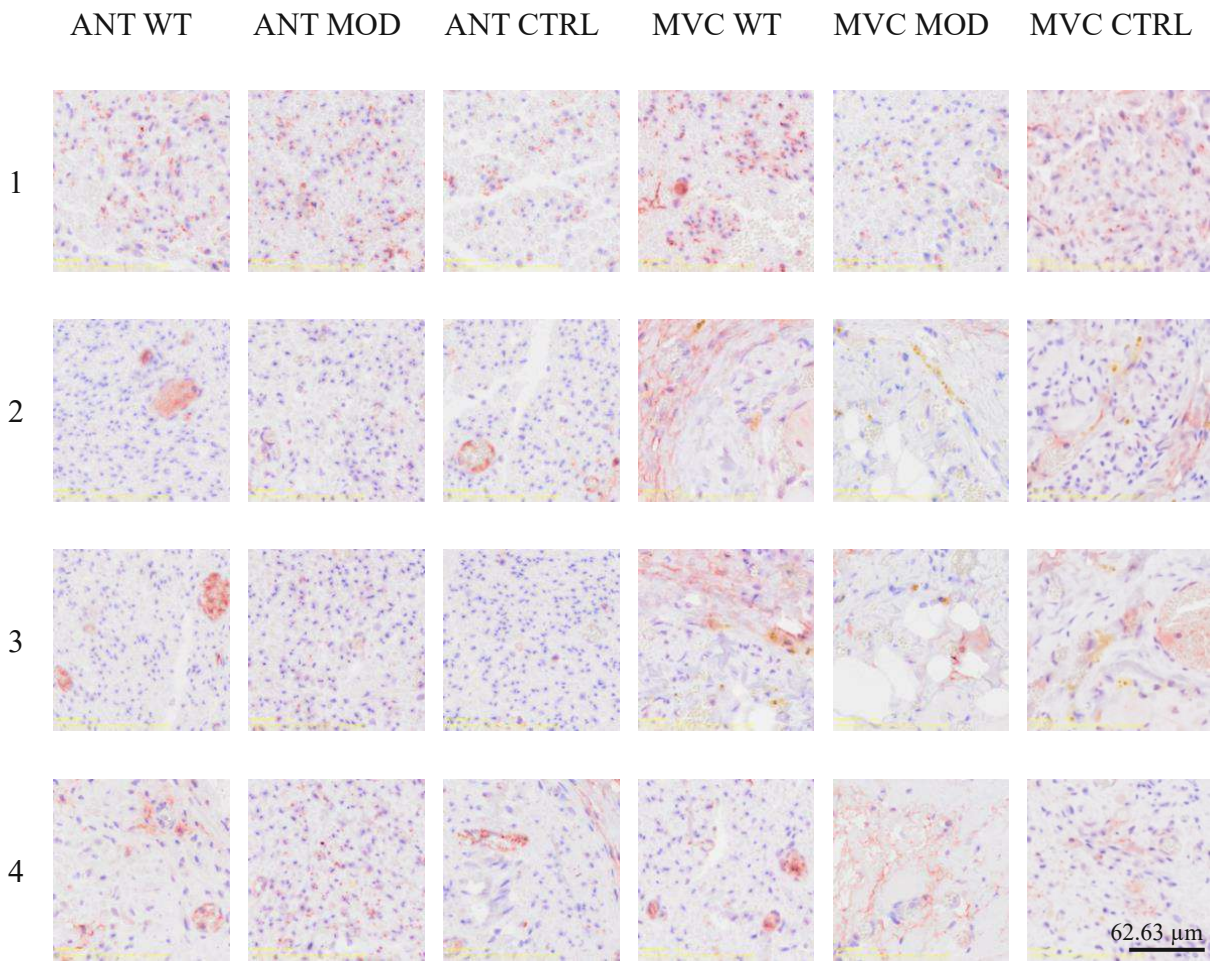

Fig. 11. GFAP staining of central regions of histological sections from four median nerve sites across autologous nerve transplant (ANT) and muscle filled-in vein conduit (MVC) with extracellular vesicle treatment. Representative bright field images of 12-week regenerated nerve with 8-week repair delay at 4 anatomical sites: (1) proximal of implant, (2) proximal of conduit middle cut, (3) distal of conduit middle cut, and (4) distal of conduit. Images are taken at the interface between muscle and vein (MVC groups cuts 2 and 3) the remaining images are taken randomly from the middle of the nerve tissue. Image identifiers can be found in Table A1.1.

3.6 MBP staining

MBP staining was used to assess myelination of delayed regenerated nerves. Both the ANT and MVC groups showed MBP-positive regions, indicating remyelination (Fig. 12). With the ANT groups displaying a denser and more continuous MBP signal compared to the MVC group. The ANT has a clear central region surrounded by a thick layer of connective tissue which contains several myelinated axon bundles, but with the largest number of axons located in the center. The MVC group exhibits very few and patchy MBP distribution in the central regions as well as in the outer layers, and has a slight increase in MBP-positive signal in the most distal segment. The nerve fibers are observed in the vein segment of the MVC conduit, and few in fascicles between the muscle tissue.

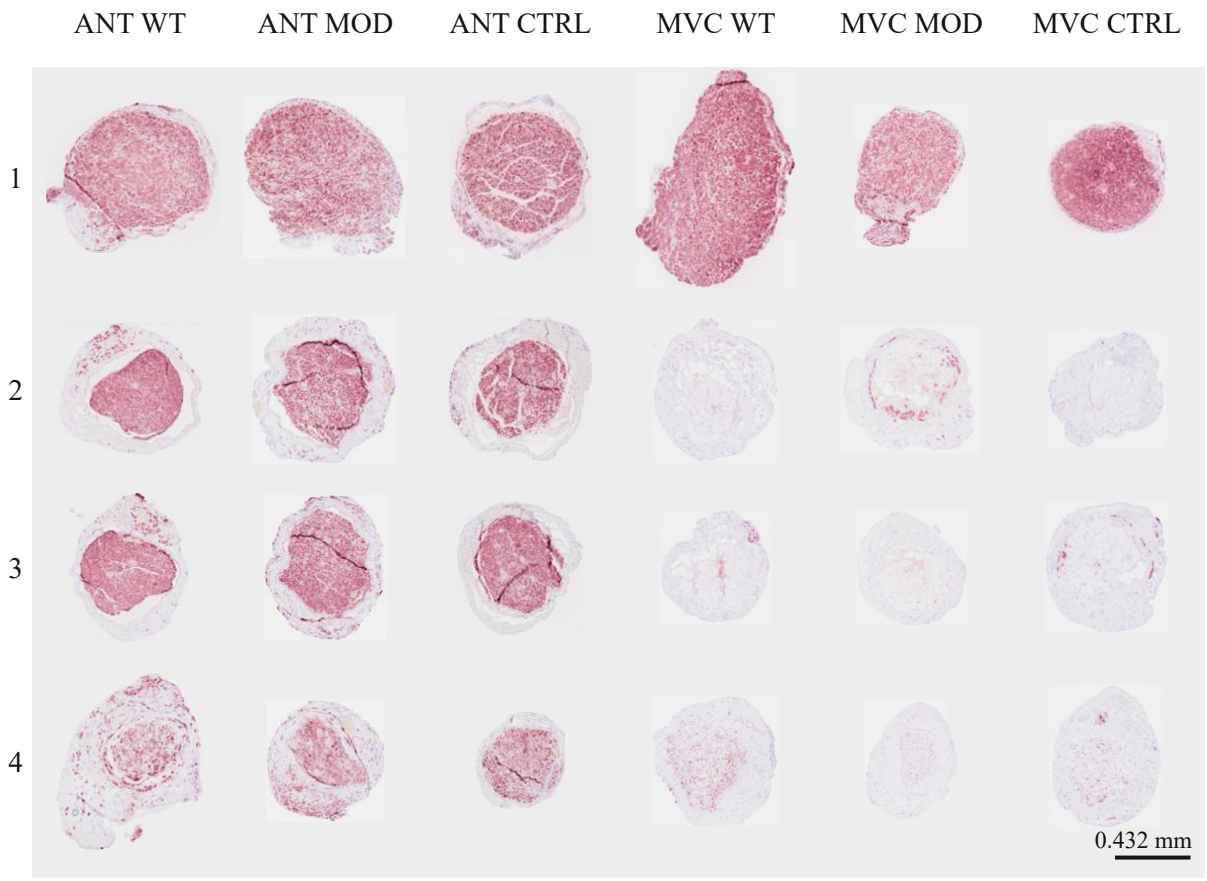

Fig. 12. MBP with Hematoxylin counterstain of median nerve across autologous nerve transplant (ANT) and muscle filled-in vein conduit (MVC) and extracellular vesicle treatment at four anatomical locations. Representative bright field images of 12-week regenerated nerve post 8-week delay at 4 anatomical sites: (1) proximal of implant, (2) proximal of conduit middle cut, (3) distal of conduit middle cut, and (4) distal of conduit. Image identifiers can be found in Table A1.1.

3.6.1 Automated segmentation of axon and myelin

To quantify axon and myelin morphology during regeneration, automated segmentation was performed using the deep learning-based tool AxonDeepSeg (ADS). Raw images yielded inconsistent segmentation quality (Fig. 13b and e). Therefore, a standardized preprocessing step was performed, including contrast enhancement, implemented prior to segmentation (Fig. 13d). Following preprocessing, ADS produced consistent accurate segmentation of axons and myelin sheaths across the various test groups with the most accurate results in the ANT treated groups compared to the MVC, due to poor regenerated structures being harder to recognize by the software (Fig. 13c and f).

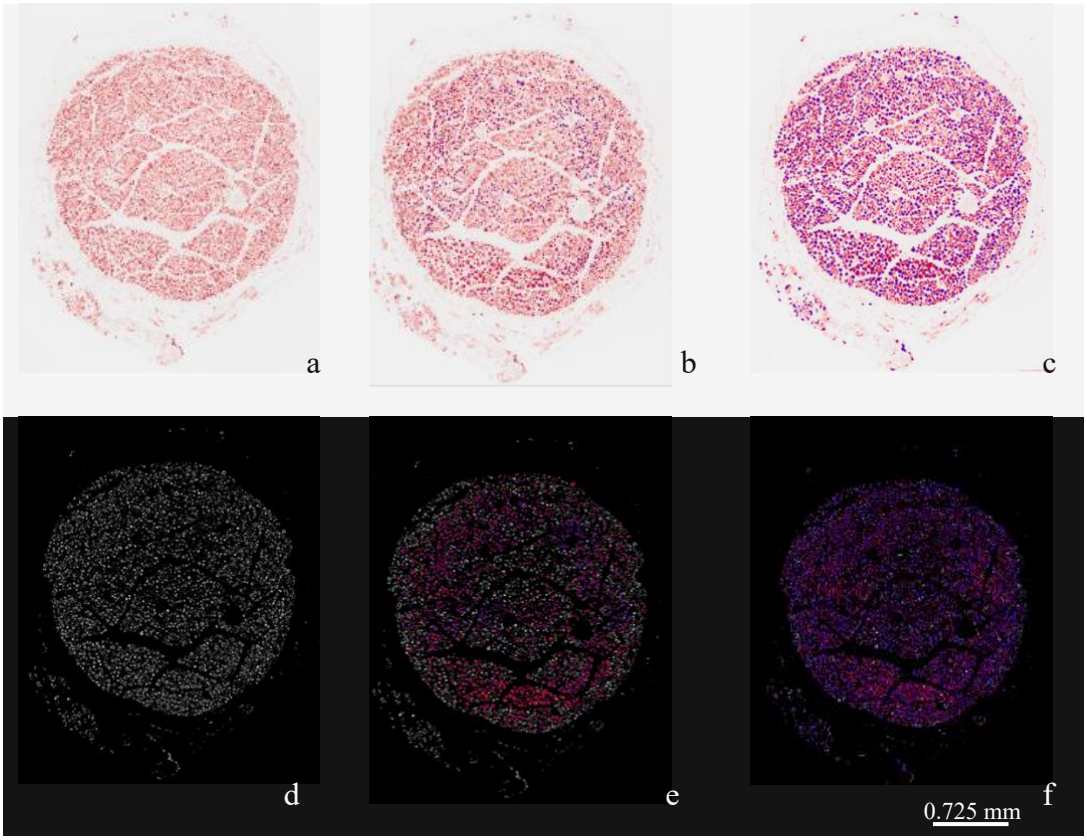

Fig. 13. AxonDeepSeg masked median nerve cross section images. (a) Original brightfield image of a cross-section stained for myelin basic protein (MBP). (d) Corresponding image after preprocessing using ImageJ. (b, e) Segmentation mask generated by AxonDeepSeg on the unprocessed image, showing axon and myelin detection. (c, f) Segmentation mask generated from the preprocessed image, demonstrating improved resolution. MBP image is from an animal (rat No. 10) of the ANT with control EV group.

Fig. 14 shows a higher magnification view of the ADS segmentation results from Fig. 13, allowing for clearer visualization of individual axons and myelin sheaths. This figure enables closer inspection of how the segmentation algorithm identifies and outlines neural structures in the preprocessed images. Compared to the overview provided in Fig. 13, the increased magnification here highlights the detailed performance of the segmentation, offering a more precise understanding of how axon and myelin boundaries are detected.

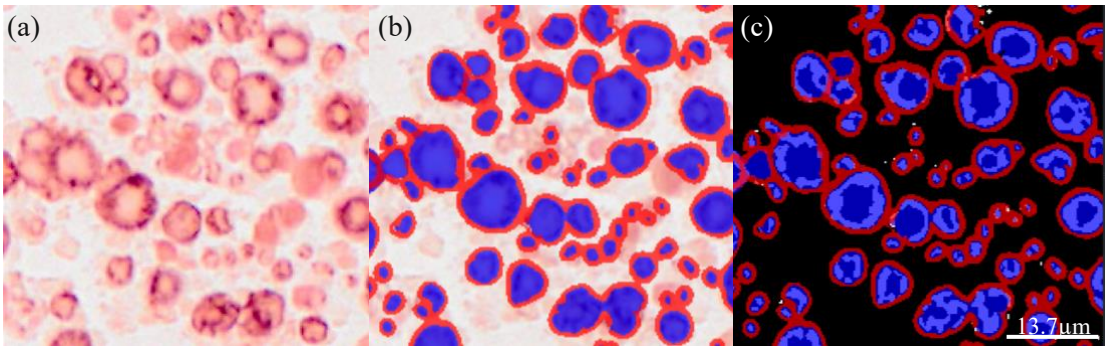

Fig. 14. Higher magnification view of AxonDeepSeg segmentation on MBP-stained nerve cross section. (a) Original brightfield image of a cross-section stained for myelin basic protein (MBP). (b) Segmentation mask generated by AxonDeepSeg on the unprocessed image, showing axon and myelin detection. (c) Corresponding image after preprocessing using ImageJ. MBP image is from an animal (rat No. 10) of the ANT with control EV group.

From the axon-myelin segmentation ADS allowed for histomorphometric calculation of all cuts, which resulted in a CSV file including: the coordinates of the axon, axon diameter, g-ratio, myelin thickness, and number of axons. The fiber diameter was calculated through the axon diameter and g-ratio. The morphometrics are compared between groups for each cut, the comparison between proximal and distal to the injury (cut 1 and 4) is depicted in Fig. 15. All parameters for each cut are organized in the appendix images A1.2-A1.5. The total number of myelinated axons decreases from proximal to distal of the injury, however, for the ANT this difference is insignificant whereas for the MVC this is a significant difference. Also, it is noted that the proximal number of axons in the MVC is greater than in the ANT (table 3). The same results are found for the nerve fiber density as this relates to the total amount of axons. Slightly smaller fiber diameters are found for the proximal cut compared to the distal cut, which is reversely observed in the g-ratio where the g-ratio is greater proximally than distally (Fig. 15d and f).

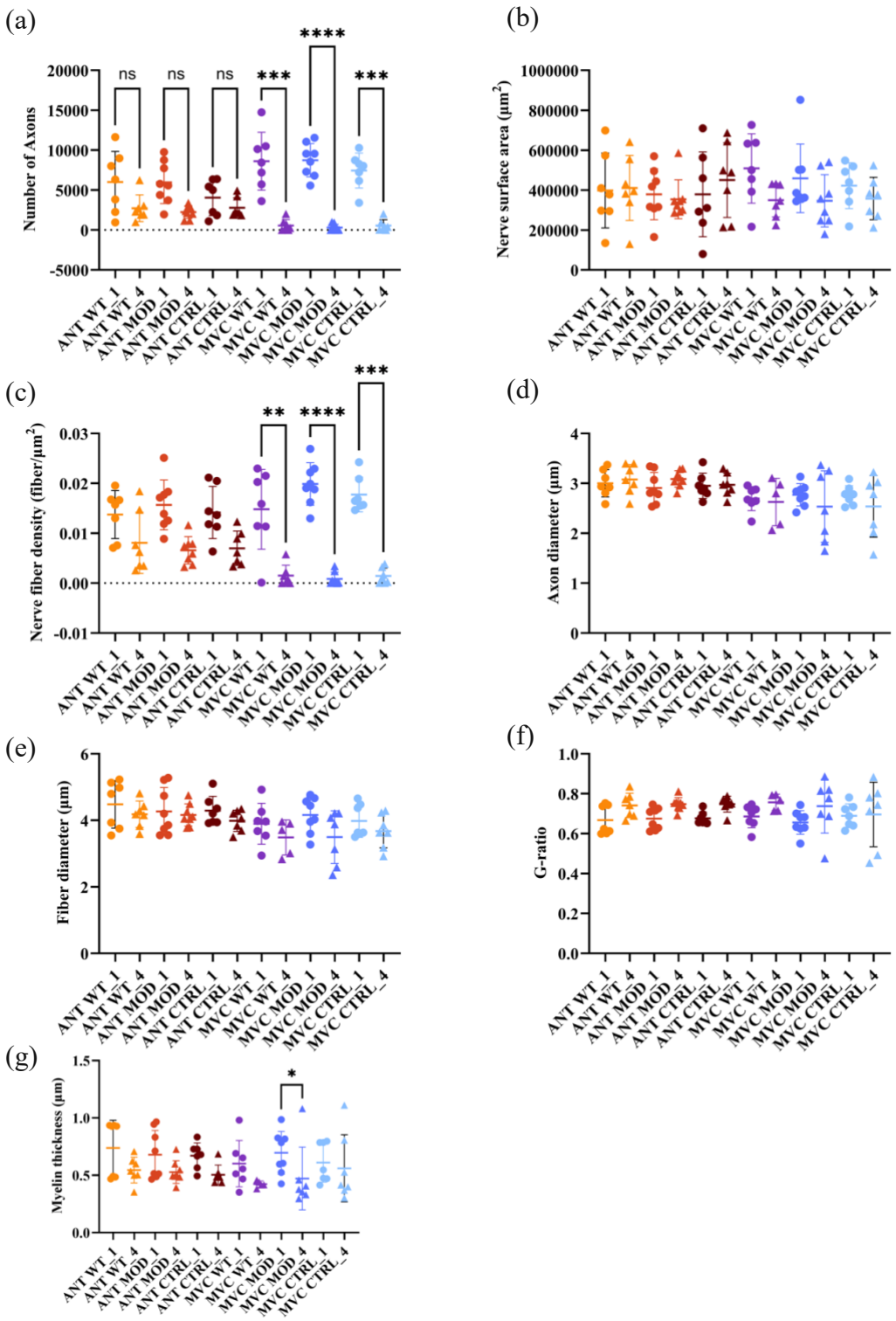

Fig. 15. Histomorphometric data of the treatment groups comparison at proximal and distal median nerve locations. The data is calculated from MBP stained images from anatomical sites proximal (1) and distal (4) to the injury. (a) total number of nerve fibers, (b) nerve surface area, (c) nerve fiber density, (d) axon diameter, (e) fiber diameter, (f) G-ratio, and (g) myelin thickness. Statistical significance was assessed with the Brown-Forsythe and Welch test followed by Dunnett's T3 multiple comparisons test (*p<0.05, **p<0.01, ***p<0.001, ****p<0.0001).

Table 3: Descriptive statistic of histomorphometric parameters for MVC and ANT across EV treatment groups

		Wildtype EV		Modified EV		Control	
		ANT	MVC	ANT	MVC	ANT	MVC
Number of axons (N)	Proximal (cut 1)	6001± 3851	8615± 3623	5960± 2653	8747± 2086	4051± 2250	7451± 2187
	Mid graft (cut 3)	4491± 2176	268± 549.5	4644± 1045	38.25± 58.99	3897± 843.1	110± 159.7
	Distal (cut 4)	2727± 1682	559.7± 734.2	2237± 790.1	293.4± 418.4	2783± 1250	551.1± 719.7
Axon diameter (µm)	Distal (cut 4)	3.080± 0.2975	2.627± 0.4743	3.090± 0.1659	2.535± 0.7167	2.972± 0.2306	2.538± 0.6158
Myelin thickness (µm)	Proximal (cut 1)	0.7387± 0.2409	0.6019± 0.2019	0.6792± 0.2117	0.6954± 0.1867	0.6709± 0.1119	0.6106± 0.1716
	Distal (cut 4)	0.5459± 0.1125	0.4226± 0.02863	0.5281± 0.09855	0.4721± 0.2736	0.5041± 0.0853	0.5609± 0.2927

Note. EV treatment groups included modified EVs, wildtype EVs, and vehicle control.

The distribution of axon and fiber diameters for the ANT groups is shown in Fig. 16 and 17. Across all anatomical levels (cuts 1-4), axons diameters most commonly ranged between 2 and 3 µm, while fiber diameters peaked around 4 µm and exhibited a slight leftward shift. No notable differences in the diameter distribution patterns were observed between the different cuts or treatment groups, suggesting a consistent morphological profile throughout the nerve. Corresponding data for the MVC group can be found in the appendix (Fig. A1.6 and A1.7).

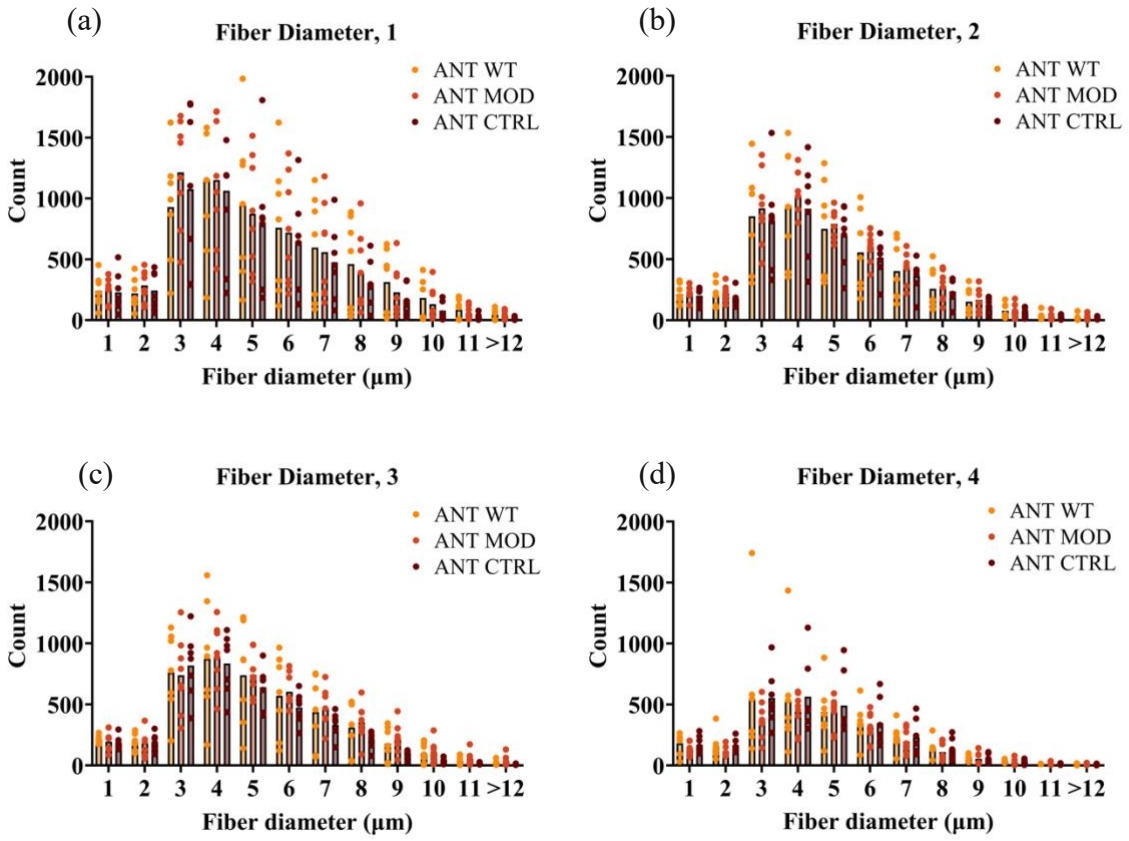

Fig. 16. Histogram representation of fiber diameter distribution between the treatment groups in the anatomical cuts. Yellow represents the ANT + wtEV group, orange the ANT + modEV group, and brown the ANT + control vehicle group. The cuts are located proximal from the injury (1), proximal of the middle of the injury (2), distal of the middle of the injury (3), and distal from the injury (4).

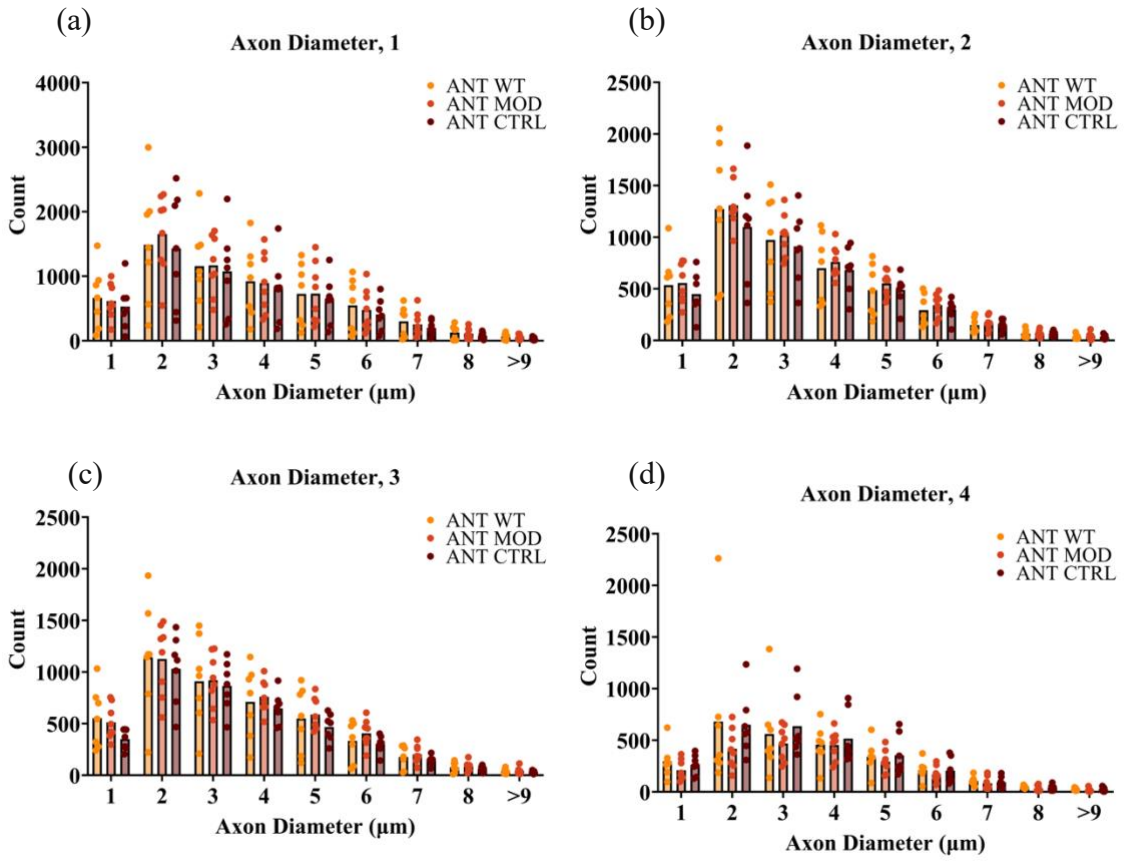

Fig. 17. Histogram representation of axon diameter distribution between the treatment groups in the anatomical cuts. Yellow represents the ANT + wtEV group, orange the ANT + modEV group, and brown the ANT + control vehicle group. The cuts are located proximal from the injury (1), proximal of the middle of the injury (2), distal of the middle of the injury (3), and distal from the injury (4).

3.7 MSB staining and muscle analysis

MSB-stained cross-sections of the FDS muscle revealed clear differences in tissue composition across treatment groups following median nerve injury and regeneration (Fig. 18). Color deconvolution of the staining allowed for visualization and quantification of muscle and connective tissue components (Fig. 19). Analysis showed varying levels of fibrin and collagen content, with some groups displaying pronounced muscle atrophy and increased connective tissue, while other preserved more muscle fibers (Fig. 20). These differences reflect the extent of functional nerve regeneration, with better outcomes associated with reduced fibrosis and greater muscle integrity. As expected, the ANT groups demonstrated larger amounts of muscle tissue in the FDS on the repaired side (right) and greater amounts of connective tissue on the

injured non-repaired side (left). The largest amount of muscle fiber was found in the groups receiving EV treatment (both wildtype and modified). The MVC treated groups demonstrated inconsistent results between animals, but most showed large amounts of connective tissue (Fig. 18).

ANT treated animals demonstrated greater right FDS muscle weights (ANT + wtEV: 0.162 ± 0.02001g, ANT + modEV: 0.161± 0.03011g, ANT + CTRL: 0,151± 0.01943g) versus MVC (MVC + wtEV: 0.08943 ± 0.03857g, MVC + modEV: 0.07538± 0.03760g, MVC + CTRL: 0.09786 ± 0.02914g) (Fig. 21b), and achieved greater muscle regrowth towards the healthy muscle weight (ANT + wtEV: 67.23± 8.303%, ANT + modEV: 66.76 ± 12.50%, ANT + CTRL: 62,67 ± 8.065%) compared to MVC treated animals (MVC + wtEV: 37.11± 16.01%, MVC + modEV: 31.28 ± 15.60%, MVC + CTRL: 40.61 ± 12.09%) (Fig. 21d). Spearman's correlation showed a significant correlation between left FDS muscle weight and muscle surface area (r=0.3859, p=0.0097).

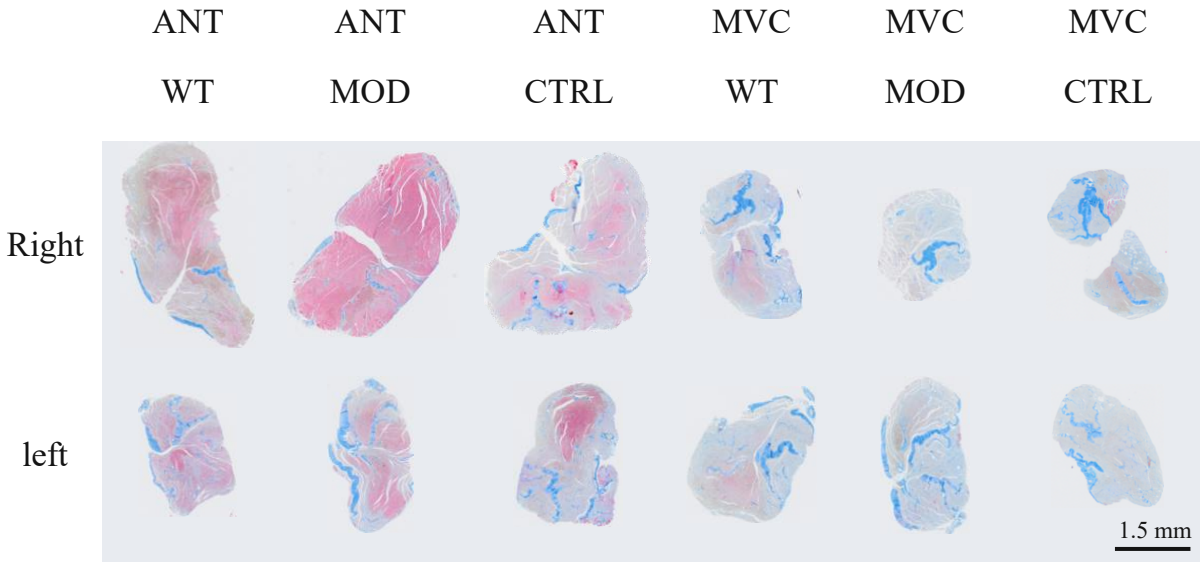

Fig. 18. MSB staining of right and left FDS muscle with autologous nerve transplant (ANT) or muscle filed-in vein conduit (MVC) and different extracellular vesicle treatments. Representative bright field images of 8 week denervated and 12-week potentially re-innervated muscles (upper row) and 12 week denervated muscles (lower row). Image identifiers can be found in Table A1.1.

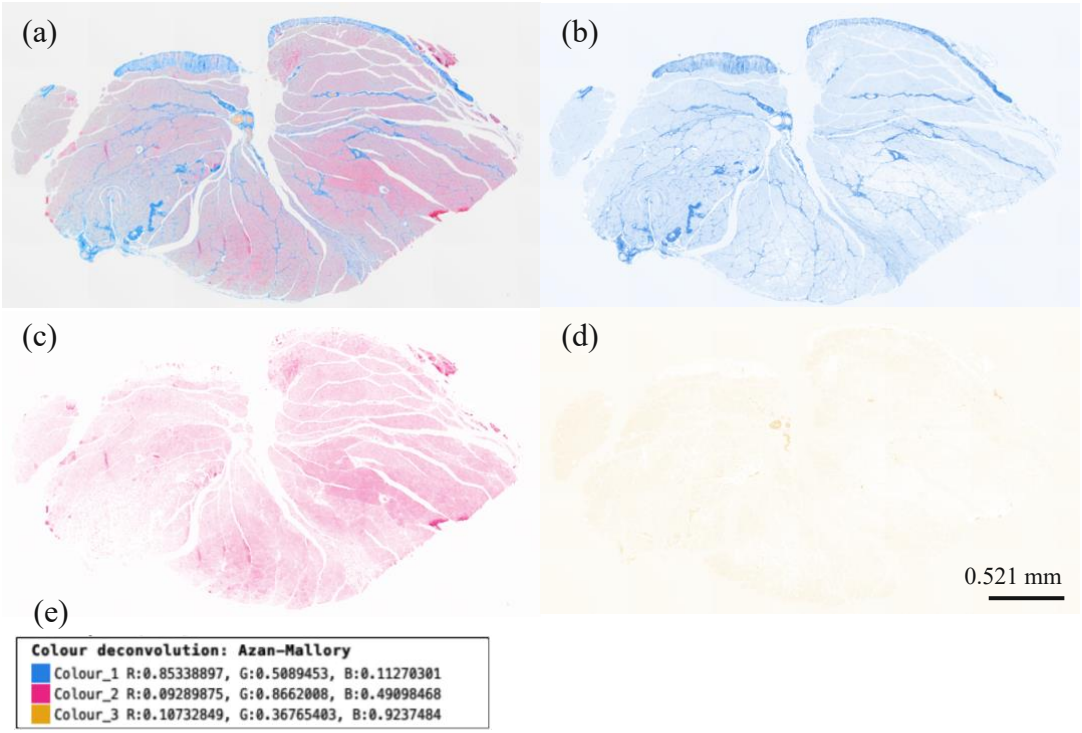

Fig. 19. MSB stained cross-section of the right FDS muscle from an animal (rat No. 5) in the ANT Control EV group. The image was processed using Colour Deconvolution in ImageJ with Azan-Mallory vectors, separating the MSB stain into its constituent components (e): (b) collagen (blue), (c) muscle fibers/fibrin (red/pink), and (d) erythrocytes (yellow).

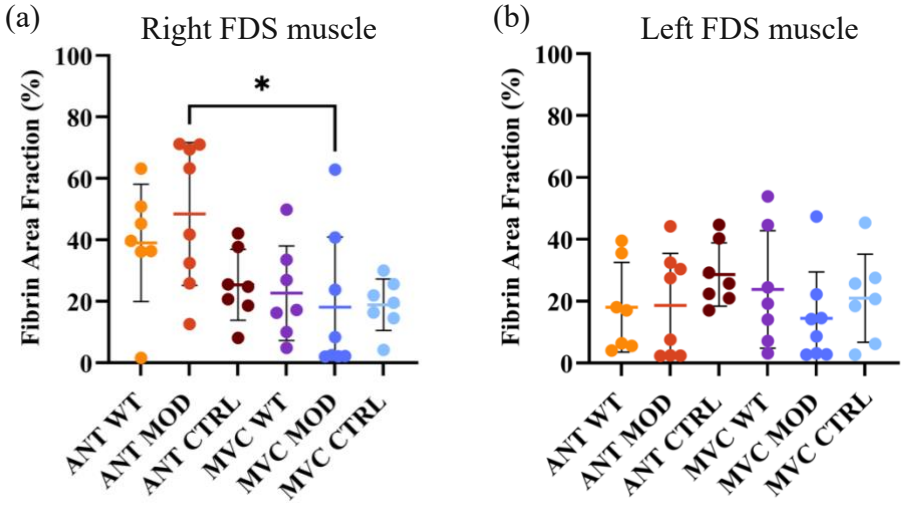

Fig. 20. Fibrin area fraction of total FDS muscle. (a) Fibrin area fraction of right FDS muscle with the different grafts and EV treatments, (b) fibrin area fraction of left 12-week denervated FDS muscle. Statistical significance was determined using ANOVA followed by the Kruskal-Wallis multiple comparison test (*p<0.05).

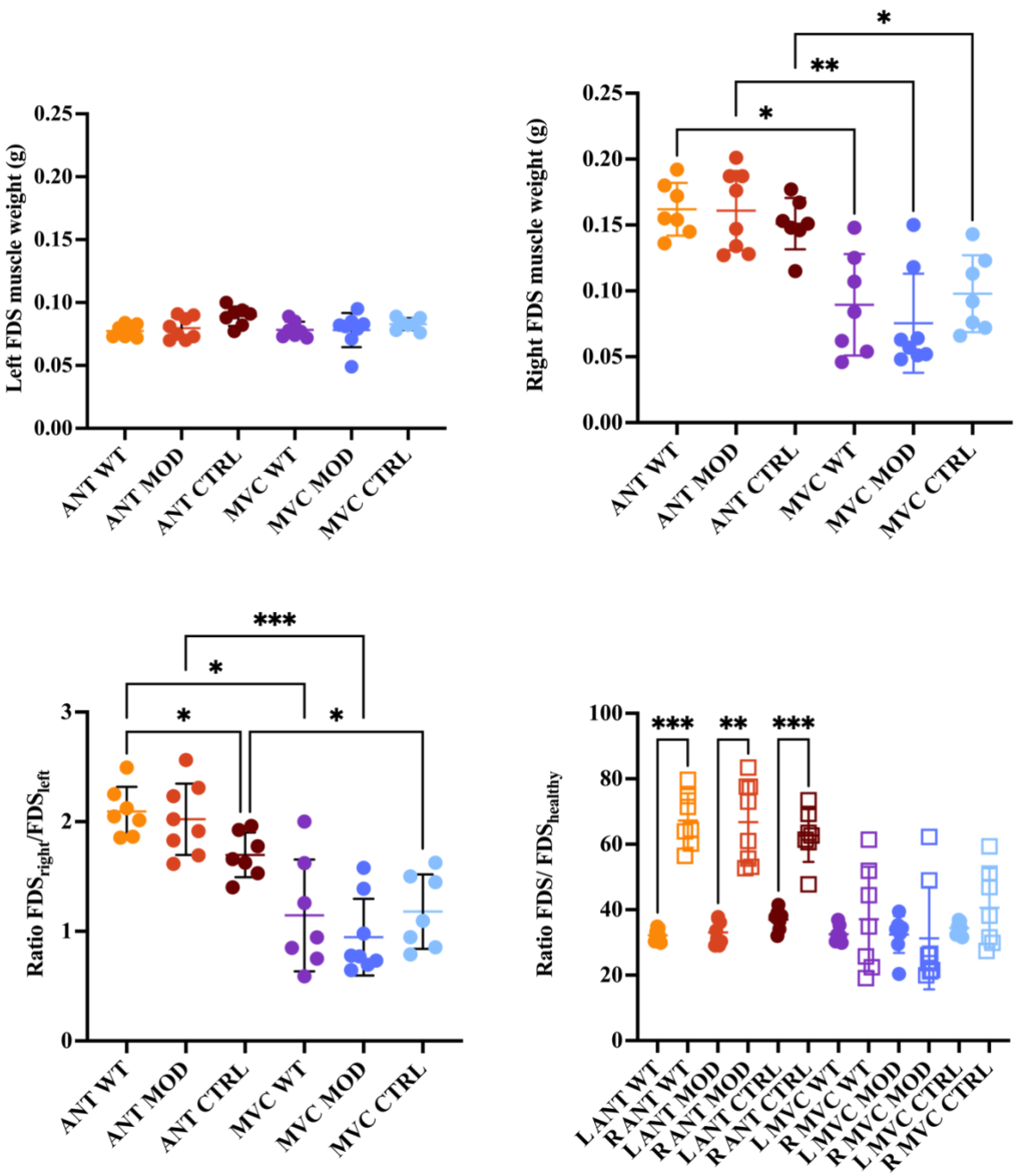

Fig. 21. FDS muscle weight analysis. (a) left FDS muscle weight, (b) right FDS muscle weight. (c) ratio between right and left FDS muscle, (d) Percentage of right FDS muscle weight to healthy FDS muscle. Statistical significance between ANT and MVC was assessed with the Brown-Forsythe and Welch test followed by Dunnett's T3 multiple comparisons test (*p<0.05, **p<0.01, ***p<0.001 between ANT and MVC).

3.8 Correlation of Histomorphometry and Electrophysiology

The *P* values obtained by the *F* statistic applied to find significant correlations between the histomorphometric and electrophysiological data after performing a simple linear regression analysis are shown in Table 4. Significant linear correlations with $p<0.05$ could be found for 11 cases (Fig. 22). These were between (a) CMAP duration and total amount of fibers ($y = 0.0005243 \times X + 4.785$) (b) CMAP amplitude and total amount of fibers ($y = 0.002102 \times X + 3.828$), (c) CMAP Area under the curve and total amount of fibers ($y = 0.001550 \times X + 3.168$), (d) CMAP amplitude and nerve fiber density ($y = 556.2 \times X + 4.661$), (e) CMAP area under the curve and nerve fiber density ($y = 399.9 \times X + 3.825$), (f) CMAP duration and axon diameter ($y = 2.272 \times X - 0.7041$), (g) CMAP amplitude and axon diameter ($y = 5.070 \times -6.829$), (h) CMAP area under the curve and axon diameter ($y = 3.758 \times X - 4.717$), (i) CMAP amplitude and fiber diameter ($y = 3.371 \times X - 5.520$), (j) CMAP duration and G-ratio ($y = 12.67 \times X - 3.635$), and (k) CMAP duration and myelin thickness ($y = -4{,}670 \times X + 8.092$). Only statistically significant correlations between histomorphometric parameters and electrophysiological data are reported in the main text. A complete overview of non-significant correlations can be found in Appendix Fig. A1.8 and A1.9.

Table 4: F statistic of simple linear regression analyses between the histomorphometric and Neurographic data

	Neurographic parameters			
	Latency	**Duration**	**Amplitude**	**Area under the curve**
Histomorphometric parameters				
Total amount of fibers (N)	0.0992	0.0386*	0.0002*	0.0005*
Cross sectional area	0.5609	0.3564	0.0731	0.0833
Nerve fiber density	0.8540	0.1283	0.0036*	0.0086*
Axon diameter	0.3586	0.0014*	0.0026*	0.0050*
Fiber diameter	0.3266	0.1707	0.0302*	0.0618
G-ratio	0.8458	0.0011*	0.0964	0.0732
Myelin Thickness	0.8258	0.0241*	0.4949	0.3746

The numbers correspond to *P* values. Significant values ($p<0.05$) are marked with an asterisk.

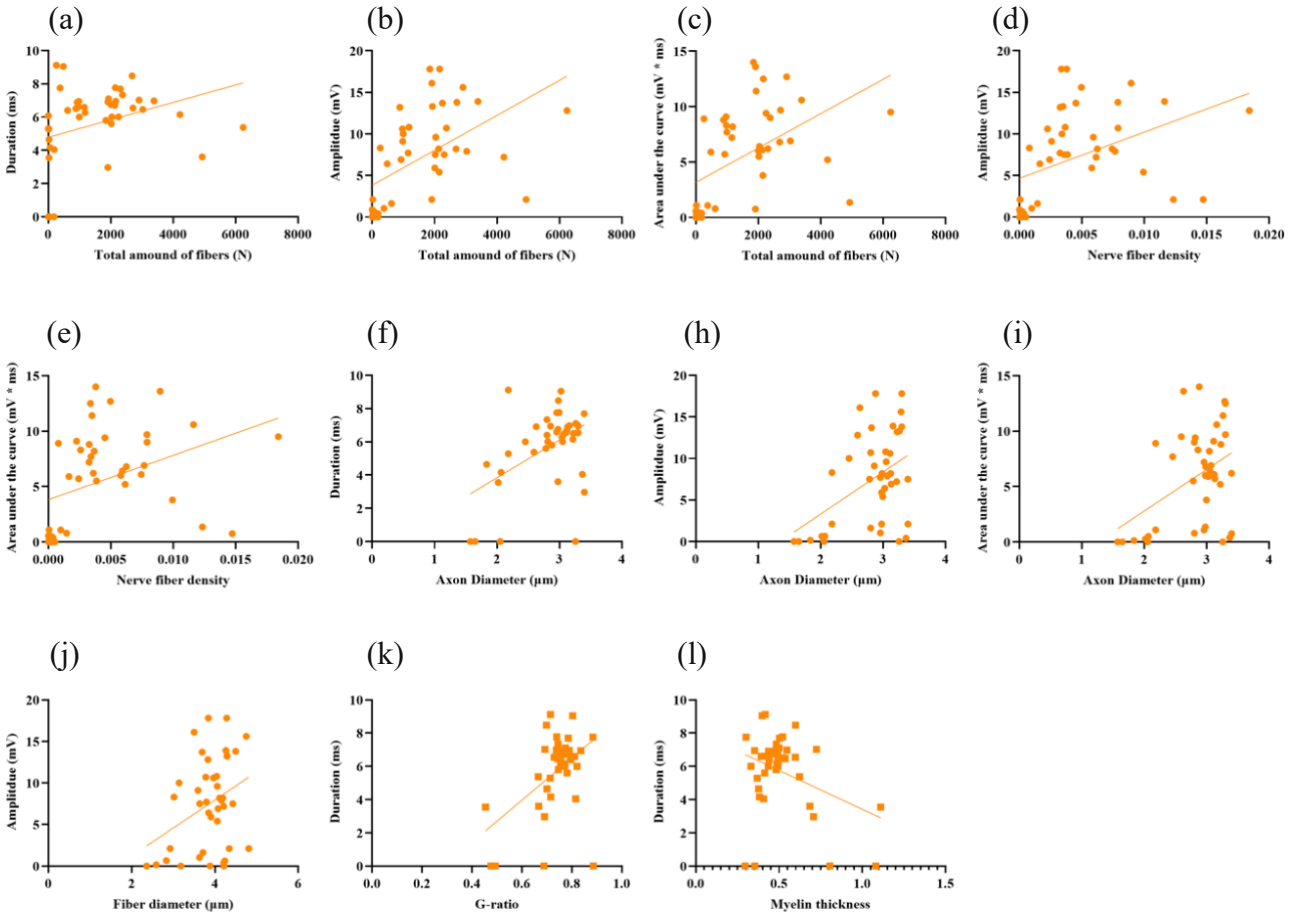

Fig. 22. Significant linear correlations plot between histomorphometric and electrophysiological parameters.

4 Discussion

The current study was conducted with the aim to assess the regeneration potential of a 7-mm median nerve gap with MVCs compared to the golden standard of the ANT with additional EV (wildtype, modified, and control) therapy. This study investigated nerve regeneration by combining electrophysiology with muscle weighing, immunohistochemistry, and histomorphometry.

4.1 Electrophysiology

No significant differences were found between the ANT and MVC regarding the latency and duration, representing the fastest conducting nerve fibers and the consistency of the type of motor fiber. A mean difference in CMAP amplitude and area under the curve is found between the ANT and the MVC confirmed by a significant difference between ANT + modEV and MVC + modEV. The improved outcome in CMAP of the ANT compared to the MVC are coherent with literature, but values cannot be directly compared while they opted for a non-invasive method [48]. No significant differences were found between the EV treatments groups, due to a large variation between animals within the groups. The CMAP values obtained in this study can be compared to those reported by Wang et al. [38]. In their baseline measurement, they recorded an onset latency of 1.5 ms, an amplitude of 8,2 mV, a duration of 1.3 ms, and an area of 4.7 mV* ms. They also presented data from four weeks post-operation, revealing an onset latency of 10.1 ms, an amplitude of 0.1 mV, a duration of 12.3 ms, and an area of 0.5 mV* ms. From this comparison, it is evident that the latencies and ANT amplitudes found in our experiment are similar to the baseline measurement described by Wang et al. [38]. However, the durations in our findings are longer and align more with the results observed in Wang et al.'s four-week post-operative data. A significant difference between the two experiments lies in the method of nerve repair; Wang et al. transected the median nerve and immediately repaired it through primary neurorrhaphy; therefore, they did not use a gap conduit.

The electrophysiology results should be interpreted cautiously due to several study limitations. During the electrophysiology assessments, different nerve morphologies were observed; some animals exhibited thinned nerves near the sutures, while others did not. This difference could have arisen from the placement of the sutures or the animals' physical activities post-surgery. Additionally, nerve thinning might have occurred when positioning the nerve onto the stimulation electrodes and clearing it from surrounding areas. The micromanipulator setup with

the stimulating electrode had inconsistent stability, which led to instances where the nerve was abruptly stretched, potentially causing plastic deformation in its underlying structures. Consequently, this could impair nerve conduction, meaning the results might not accurately reflect true regeneration [39]. To mitigate this limitation, it's essential to practice the procedure and ensure the stability micromanipulator and the stimulating electrode fixture. Achieving this can be done by carefully organizing the surgery table and providing plenty space for the electrode setup. This limitation is not only related to the electrode placement but also is relevant for the repair surgery. In the surgery, it is possible that the nerve is stretched, this causes tension and when exceeding about 8% of elongation there is a change of inducing detrimental effects on nerve repair, in which for example SC activation is inhibited preventing axonal regeneration [62].

Additionally, the metals of the stimulating electrode were bendable, causing an inconsistent distance between the anode and cathode. This might result in differences in CMAP data as it can influence the threshold and amount of fibers it activates [63]. This can be resolved with the use of a more substantial stimulating electrode less prone to bending, where the distance can be standardized.

One major limitation was the electrode placement in the FDS muscle. During the measurement this electrode could move due to physical movement of the muscle which resulted in changes in the electrophysiology data, reinsertion then also resulted in different CMAP results showing the high variability due to electrode placement. This issue is not easily resolved other than that the researcher must thoroughly analyze the results during the experiment and frequently check the placement in the FDS. A precaution taken was that only one researcher carried out the electrode placement to minimize the variability between different researchers.

The analysis itself also came with limitations as the equipment is designed for clinical assessment where the raw data is not needed for diagnosis. The software therefore does not allow for raw data extraction of the individual curves for each stimulus, resulting in the values needing to be extracted manually. As the software does not estimate the end of the action potential very well, this must be determined by the researcher which can cause errors. It is attempted to limit these errors by the extraction of data being performed only by one researcher. The same limitation applies to the extraction of the latency and duration, as they are not simply the maximum value obtained with increasing stimuli, but rather the average of the plateau. Not all results were as straightforward to analyze possibly causing slight differences. These differences are expected to be very minimal and should not change the final conclusions.

The electrophysiology did not show significance between the treatment groups except for the difference between MVC and ANT. The animals were part of a larger study that included functional assessment over the 12-week period using grip strength testing. Following electrophysiological measurements, the animals were sacrificed, and the median nerve and FDS muscle were harvested for histological analysis. These results combined will create a bigger picture and potentially show significant differences between the EV treatment groups.

To repeat this study, it would be recommended to standardize the placement and the distance between the stimulating and recording electrode and stabilize the set up to limit plastic deformations of the nerve. Alternatively, non-invasive electrophysiology could give useful insights of the regeneration process as it is one of the methods with the earliest detection of reinnervation, where the muscle conduction can be analyzed throughout the regeneration period. This would show the decrease in latency and duration and the increase in amplitude and area under the curve [38], [48], [57].

4.2 Histology

4.2.1 H&E staining

Stössel (2017) reported morphological patterns in both the ANT and MVC groups that are partially consistent with the findings in this study [48]. Specifically, they observed increased loose connective tissue surrounding the epineurium in the ANT group and residual muscle tissue in the MVC group, findings that align with our observations. However, they noted that all remaining muscle tissue had disappeared after 12 weeks post repair, which contrasts with our results, where muscle remnants were still clearly detectable at the same time point [48]. Furthermore, Stössel did not report any presence of adipose tissue, whereas our H&E staining revealed distinct adipose deposits, particularly in the ANT group. Notably, other studies have also observed persistence of grafted muscle fibers that did not fully degenerate and remained visible at the time of analysis [64], [65]. Consistent with previous research [66], the MVC group in our study exhibited a higher concentration of muscle tissue in the central regions of the graft compared to the periphery, suggesting region specific preservation or regeneration patterns.

4.2.2 c-Jun staining

C-Jun staining was most prominent in the proximal part of the median nerve and was rarely found in the MVC group (Fig. 10). This pattern reflects the biological role of c-Jun as a

transcription factor upregulated in SCs following peripheral nerve injury. Since the MVC construct lacks native SCs, c-Jun expression in this group would require SC migration into the conduit, which appears limited. In contrast, the proximal and distal attachments of the conduit (anatomical sites 1 and 4) consist of native median nerve tissue that contains resident SCs, which explains the localized c-Jun expression at these regions.

The ANT groups demonstrated c-Jun activity throughout the graft, with positive staining observed at all anatomical locations. Among these, the ANT + wtEV group exhibited the most consistent c-Jun activity across animals, while the ANT+ modEV group showed high inter-animal variability, ranging from complete absence to widespread expression of c-Jun. While overall c-Jun activity was higher in the ANT groups compared to MVC, no direct correlation between c-Jun expression and regenerative outcome could be established, particularly regarding the modified ANT group. This indicates that c-Jun expression alone may not reliably predict the degree of regeneration.

It is important to note that while c-Jun is often used as a marker of SC activation, it is not exclusive to SCs; other cell types involved in injury responses and regeneration, such as fibroblasts and macrophages, can also express c-Jun. this underscores the need for caution when interpreting c-Jun staining in complex tissue environments.

Moreover, c-Jun is known to be rapidly upregulated within the first two weeks post-injury and declines thereafter [67], [68]. Downregulation of c-Jun is a prerequisite for remyelination, as it functions as a negative regulator of myelination [55]. Given that c-Jun staining in this study was performed 20 weeks post-injury, the observed expression likely reflects heterogeneous regenerative states among animals. Some animals may still be undergoing active regeneration, while others may have progressed to later stages where c-Jun expression has diminished.

Due to the qualitative nature of the current assessment and the variability of c-Jun expression, establishing a clear link with functional outcomes such as electrophysiological recovery remains challenging. Future studies should incorporate quantitative analysis of c-Jun expression, ideally in combination with other markers of regeneration and myelination, to more accurately determine the stage of regeneration and the role of c-Jun in this process.

4.2.3 GFAP staining

GFAP-positive staining can reflect various SC stages following nerve injury and regeneration. In uninjured peripheral nerves, GFAP is primarily expressed by non-myelinating SC,

particularly Remak cells. After injury or during SC dedifferentiation, GFAP expression is upregulated, especially during the early regenerative phase, making GFAP a marker for immature/dedifferentiated SCs and transient repair SCs with a pro-regenerative phenotype [69]. However, due to these overlapping expression profiles, a single GFAP staining alone cannot reliably distinguish between these SC subtypes.

To better localize non-myelinating SCs, an attempt was made to overlay GFAP and MBP staining images to visualize their spatial relationship. The aim was to identify GFAP-positive cells situated between myelinated axons. However, the overlay was technically limited: GFAP signal intensity was relatively low, and the images were taken from non-consecutive tissue sections, resulting in imperfect alignment. Consequently, the composite images did not permit a clear anatomical distinction between GFAP- and MBP- positive regions.

Qualitative assessment revealed GFAP-positive cells predominantly in the proximal nerve segment. This observation aligns with previous studies, which demonstrated that GFAP-positive SCs invade the MVC conduit from both proximal and distal stumps as early as 12 hours post-surgery, and by 115-140 hours, the graft is fully infiltrated with GFAP-positive cells [25], [70]. The proximal staining pattern observed in our study is also consistent with that of intact nerves, where GFAP labels non-myelinating SCs not associated with myelinated axons [71].

In contrast, GFAP staining within the MVC displayed more diffuse and heterogenous patterns, differing notably from the proximal nerve segment. A network-like GFAP signal was observed, but it lacked the structural organization typical of native SC arrangements. Inter-animal variability was substantial with some animals showing strong edge staining, while others had minimal edge signal and overall weak staining. Interestingly, animals with low edge signal also exhibited lower GFAP positivity throughout the tissue, suggesting strong edge effects may reflect processing artifacts rather than true biological signal. Additionally, GFAP-positive regions often corresponded to disrupted or ruptured areas observed in HE staining, further raising the possibility that some of that signal may originate from mechanical damage rather than genuine non-myelinating SCs.

4.3.4 MBP staining

MBP staining showed a clear drop in the number of myelinated axons in the MVC when moving from proximal of the injury (cut 1) which still represents native nerve tissue, to the MVC (cut 2 and 3). The appearance of the regeneration of axon in the ANT is compatible with previous studies, however the MVC did not match the morphometrical patterns found in other studies

[64]. The ANT groups displayed a peripheral localization of nerve bundles, coherent with the findings with the H&E staining, displaying most muscle tissue in the center [65], [66].

Previous studies have shown similar fiber densities between the ANT and MVC but a difference in morphology exists, with the MVC displaying regeneration characterized by fascicle formation [64], [66]. This present study also observes the presence of fascicle formation, however, it reveals that fiber densities in the MVC are significantly lower than those found in the ANT.

4.3 Histomorphometry

Histomorphometry can be expensive and time consuming. It relies on the use of osmium tetroxide to segment axon and myelin, which is a toxic substance that does not allow for the other stainings performed in this study (c-Jun, GFAP, H&E, MBP) [13], [54]. AxonDeepSeg is an opensource software that has been proven to give accurate segmentations for brightfield images stained with osmium + toluidine blue staining [72]. This study applied the same segmentation model with myelin basic protein staining. For the MBP staining it is important to use solely the myelin stain without a counterstain, as the counterstain will stain nuclei that will come up after the preprocessing as axons, which causes the ADS to wrongly identify them. The preprocessing allows for better segmentation by the ADS program, however, the segmentation becomes inaccurate in poorly regenerated instances. In the case of poor regeneration, MBP staining is very faint causing artifacts to show up during the preprocessing thresholding stage. When ADS segments this poorly regenerated preprocessed image, artifacts are falsely marked, and results are inaccurate. In these cases, manual segmentation would give more accurate results.

Histomorphometrically analysis revealed differences in axon counts across the various group and anatomical locations (Fig. 15a). In both the ANT and MVC groups, the number of myelinated axons decreased progressively through the conduit when compared to the native proximal nerve tissue at cut 1. However, this reduction was only statistically significant in the MVC groups, suggesting poorer regenerative capacity in the MVC conduits compared to ANT [73]. The results for the ANT group are consistent with literature showing a gradual decline fiber numbers along the conduit, yet still maintaining higher axon counts than healthy controls [51].

A similar trend was previously reported by Stössel et al. (2017), where ANT grafts displayed significantly higher axon counts at distal sites compared to MVC constructs [48]. Nevertheless, the total number of myelinated axons in both ANT and MVC groups in this study was lower than those reported by Stössel et al. (2017), potentially due to methodological or biological differences.

Notably, at the proximal site (cut 1), the MVC group exhibited a higher average number of axons than the ANT group (Table 3). This may be attributed to axonal sprouting, a response observed when axons either reach a termination point or are unable to progress further. In the case of MVC conduits, the inability of axons to effectively enter the graft likely results in termination and local sprouting just before the entry point [74].

A notable finding in the MVC group was the reduction in axon number in the central portion of the conduit, followed by an increase in total fiber count at the distal segment (Table 3). Several factors may explain this pattern: axons may have initially grown into the outer vein wall and been lost during histological processing, or alternatively, tightly packed axons in the center may have dispersed more widely by the distal segment, resulting in an apparent increase in fiber number.

A statistically significant decrease in nerve fiber density between the proximal (cut 1) and distal (cut 4) sites was also observed in the MVC group, but no in the ANT group. Since no significant differences in nerve cross-sectional area were found (Fig. 15b and d), the changes in density are directly attributable to differences in axon number.

Notably, the nerve cross-sectional areas measured in this study were closer in value to healthy nerve controls (0.396 ± 0.009 mm^2) than those reported by Stössel et al. (2017) for injured and repaired nerves [48]. Axon diameter remained stable across the conduit in both groups, however, in the distal MVC segments diameters became more irregular, suggesting inconsistent or stalled regeneration (Table 3). This observation aligns with findings from Ikeda and Oka (2012), who demonstrated that successful regeneration is typically characterized by increasing fiber diameter over time [75]. The broad range of diameters seen in MVC groups may indicate delayed regeneration, where some axons are still actively growing, while others may have stagnated.

No significant differences in average fiber diameter were found across groups. However, myelin thickness was observed to decrease towards the distal end of the conduit in all groups, with the MVC+ modified EV group showing a statistically significant reduction (Fig. 15g). Despite this,

average axon and fiber diameters were in line with previously published data [48], while myelin thickness was slightly lower.

The frequency distribution histograms of the fiber and axon diameters are portraying a left shift, and match values of previous studies [76]. It is expected that with longer recovery times, a right shift towards larger nerve diameters would be observed [48], [77]. Notably, healthy controls in other studies involving the sciatic nerve show a distribution that have peaks at 4.5 and 9.5 µm, a pattern that occasionally found in fiber diameters in the distal segment after a longer regeneration period in transection-regeneration studies [48], [76], [77].

4.4 Electrodiagnostic and histomorphometric correlation

A strong correlation between the CMAP area and total amount of axons was expected and confirmed validating the ADS application with MBP staining [48].

Previous correlation studies have shown that velocity relates to fiber diameter and amplitude to the total number of fibers and size of the fibers [73], [78]. These results match the statistically significant correlations found in this study that show a strong relationship between the CMAP duration and axon diameter and the CMAP amplitude with total number of axons, axon, and fiber diameter. Latency was not significantly correlated with the axon or fiber diameter, however it would be expected to see a shorter latency with larger diameter, this relation, although not significant is observed (Fig. A1.8 and A1.9). However, since the distance between the electrodes wasn't measured and therefore this distance was not standardized, this evaluation is problematic [78]. An increase in the CMAP duration relates to temporal dispersion, where a variation in motor axon conduction velocities of the different motor fibers causes a longer duration [78]. This possibly explains the increase in duration with an increase in total number of fibers found in this study. With a larger number of fibers resulting in a greater variation in conduction velocities and therefore greater temporal dispersion leading to increased duration.

A clear correlation is found between myelin thickness and duration, where the CMAP duration decreases with an increase in myelin thickness, which is coherent with general understanding that myelination increases conduction velocity [7]. Similarly, the g-ratio, representing the degree of myelination through the ratio between fiber and axon diameter shows an increased duration with larger g-ratio. This is coherent with the fact that a larger g-ratio indicates a thinner myelin sheath relative to the axon's diameter.

The correlations found confirmed with literature that the method of segmentation using MBP and the open-source software ADS is a suitable and realistic method of histomorphometrical analysis.

4.5 MSB muscle staining

Histological analysis of the flexor digitorum superficialis (FDS) muscle using MSB staining provided valuable insight into the tissue remodeling processes following peripheral nerve injury and repair using ANTs and MVCs. In particular, the quantification of fibrin and collagen using the Colour Deconvolution plugin in ImageJ served as key indicator of post-denervation muscle pathology and the extent of recovery during reinnervation. Although MSB staining was used in this study, color deconvolution based on the Azan-Mallory matrix yielded consistent and interpretable results. Despite differences in staining protocols, the color profiles were sufficiently similar to allow effective separation of tissue components.

Collagen content, as visualized by the distinct blue staining in MSB sections, is increased in animals with poor reinnervation, and was mainly observed in MVC treated animal coherent with the second stage in muscle degeneration where muscle fibers are replaced by fat and fibrous connective tissue [79], [80].

4.6 Muscle weight analysis

The muscle analysis compares the test groups based on the right FDS muscle weight. It is expected that the groups with greater median nerve regeneration will show greater muscle weights compared to the poorly regenerated median nerves. This muscle weight is compared to the left FDS muscle which underwent a 12-week denervation-atrophy period. All groups received the same procedure on the left median nerve and therefore no significant differences between the groups were expected. In the ratio comparison of right FDS divided by the left FDS muscle, values greater than 1 are expected indicating greater right FDS muscle weights (in the case of median nerve regeneration) compared to the left FDS muscle weight (12-week denervation). This ratio indicates greater muscle reinnervation for ANT treated animals compared to MVC (Fig. 21c). Stössel et al. (2018) found a similar result in which they took the ratio between injured and non-injured site, here the ratio is <1, still with the largest values indicating the greatest muscle weight and thus muscle reinnervation [29]. A significant difference is found, between the ANT + wtEVs and the ANT + CTRL when taking the right to

left FDS muscle ratio. This result indicates an improvement in muscle reinnervation with the usage of wildtype EVs, but as the result is scaled by the contralateral side amplified effects could occur. In this case the ANT with control treatment shows a greater average contralateral muscle weight compared to the ANT with wildtype EV treatment (Fig. 21a). The average right FDS muscle is slightly heavier for the ANT with wildtype EV treatment than the ANT with control treatment causing an amplification with the contralateral side when taking the ratio (Fig 21b, c). Therefore, this method of evaluation does not come without flaws and cannot be considered as foolproof. The percentage of the right FDS muscle weight to the healthy FDS muscle weight is described by Bertelli and Mira (1995) [47]. In which significant differences between ANT and MVC are found but not within the conduit between EV treatment groups (Fig. 21d). The ANT groups regained more weight compared to previous studies and the MVC groups had results closer resembling complete excision without any type of conduit [50]. Generally, the muscle weights of graft treated sides are lower than their untreated contralateral side with ANTs resulting in greater muscle weights than tube-grafted injuries [49].

4.7 Future directions

Although positive differences in fibrin area and muscle weight were observed between the ANT control and ANT EV-treated groups, no significant differences were found between the wildtype and laminin-enhanced modified EVs. Furthermore, histomorphometric and electrophysiological analysis revealed no differences between the EV-treated groups and controls. Therefore, additional experiments are required to analyze the mechanisms by which EV treatment might enhance peripheral nerve regeneration. As regeneration is only assessed at the end of the regeneration period, no differences throughout are analyzed. Therefore, non-invasive electrophysiology could be performed as well as histology of the first days after injury and repair to analyze whether the EV treatment has enhanced SC dedifferentiation, proliferation and axonal regrowth in the beginning of the regeneration period.

This research has revealed promising results for the use of the open-source software ADS in combination with more accessible and affordable immunostaining with MBP. However, based on the results much progress can still be made. The preprocessing already benefited the segmentation tremendously; however further optimization can push the accuracy of the segmentation to the next level. Additionally, ADS allows for training the model on specific images, which ultimately would be the next step to have a model working specifically for MBP

stained images. From there the model needs to be validated and tested on other nerve segments before it can be implemented as a standardized method in PN regeneration assessment.

5 Conclusion

The primary aim of this thesis was to investigate the regenerative potential of extracellular vesicles derived from adipose-derived stem cells, with modifications to enhance the laminin binding in the context of peripheral nerve repair over a gap defect of 7 mm in the rat median nerve model. The goal was to improve nerve regeneration primarily to enhance functional recovery in a delayed repair setting and to advance the effectiveness of non-autologous nerve transplants to a level at which they may become competitive with autologous nerve transplantation (ANT). A secondary objective was to establish a new pipeline for histomorphometric analysis using open-source software ADS in combination with MBP staining, with the goal of enabling efficient, reproducible, and financially accessible assessment of nerve regeneration.

Overall, rat median nerve reconstruction with ANTs resulted in more complete axonal regeneration than reconstruction of the nerve lesions using MVCs. No significant differences were found between the EV treatments groups in any of the assessment methods, therefore no conclusions can be made on the functionality of these treatments. A significant difference however was found between the ANT and MVC, where the ANT showed superior results in electrophysiology, histomorphometry, muscle weight, and fibrin area. Regarding histology, ANT portrayed typical morphology with a layer of connective tissue surrounding the densely axon populated center with H&E staining. The MVC groups displayed preserved muscle tissue and substantial adipose tissue formation in the layer around the muscle tissue. C-Jun activity was found more pronounced in the center of the ANT graft compared to the MVC conduit, however, the ANT group also showed that no clear relation between functional regeneration (with electrophysiology) and c-Jun expression was found. GFAP-staining was successful in the proximal segment and in the whole ANT, however, was inconclusive within the MVC conduit, requiring alternative immunohistochemical stainings to obtain a better overview of the cellular mechanisms at hand.

The histomorphometric analysis pipeline appeared successful, demonstrating expected correlations with electrodiagnostic data. Manual segmentation will be the next step to validate the use of ADS for MBP-stained images, supporting the extension of histomorphometric analysis from peripheral to central nervous system applications.

References

[1] T. Huckhagel, J. Nüchtern, J. Regelsberger, and R. Lefering, 'Nerve injury in severe trauma with upper extremity involvement: evaluation of 49,382 patients from the TraumaRegister DGU® between 2002 and 2015', *Scand J Trauma Resusc Emerg Med*, vol. 26, p. 76, Sept. 2018, doi: 10.1186/s13049-018-0546-6.

[2] M. Wilcox, H. Gregory, R. Powell, T. J. Quick, and J. B. Phillips, 'Strategies for Peripheral Nerve Repair', *Current Tissue Microenvironment Reports*, vol. 1, no. 2, p. 49, Apr. 2020, doi: 10.1007/s43152-020-00002-z.

[3] S. Jones, H. M. Eisenberg, and X. Jia, 'Advances and Future Applications of Augmented Peripheral Nerve Regeneration', *International Journal of Molecular Sciences*, vol. 17, no. 9, Art. no. 9, Sept. 2016, doi: 10.3390/ijms17091494.

[4] K. D. Bergmeister *et al.*, 'Acute and long-term costs of 268 peripheral nerve injuries in the upper extremity', *PLoS ONE*, vol. 15, no. 4, p. e0229530, Apr. 2020, doi: 10.1371/journal.pone.0229530.

[5] M. G. Burnett and E. L. Zager, 'Pathophysiology of peripheral nerve injury: a brief review', May 2004, doi: 10.3171/foc.2004.16.5.2.

[6] H. J. Seddon, 'A classification of nerve injuries', *British medical journal*, vol. 2, no. 4260, p. 237, 1942.

[7] B. Garbay, 'Myelin synthesis in the peripheral nervous system', *Progress in Neurobiology*, vol. 61, no. 3, pp. 267–304, June 2000, doi: 10.1016/S0301-0082(99)00049-0.

[8] K. S. Topp and B. S. Boyd, 'Structure and Biomechanics of Peripheral Nerves: Nerve Responses to Physical Stresses and Implications for Physical Therapist Practice', *Physical Therapy*, vol. 86, no. 1, pp. 92–109, Jan. 2006, doi: 10.1093/ptj/86.1.92.

[9] M.-S. Ju, C.-C. K. Lin, and C.-T. Chang, 'Researches on biomechanical properties and models of peripheral nerves - a review', *JBSE*, vol. 12, no. 1, pp. 16-00678-16–00678, 2017, doi: 10.1299/jbse.16-00678.

[10] M. A. Reina, X. Sala-Blanch, R. Arriazu, and F. Machés, 'Microscopic Morphology and Ultrastructure of Human Peripheral Nerves', in *Nerves and Nerve Injuries*, Elsevier, 2015, pp. 91–106. doi: 10.1016/B978-0-12-410390-0.00007-X.

[11] J. Chato-Astrain, Ó. D. García-García, F. Campos, D. Sánchez-Porras, and V. Carriel, 'Basic Nerve Histology and Histological Analyses Following Peripheral Nerve Repair and

Regeneration', in *Peripheral Nerve Tissue Engineering and Regeneration*, Springer, Cham, 2021, pp. 1–37. doi: 10.1007/978-3-030-06217-0_14-1.

[12] E. J. Arroyo and S. S. Scherer, 'On the molecular architecture of myelinated fibers', *Histochemistry*, vol. 113, no. 1, p. 0001, 2000, doi: 10.1007/s004180050001.

[13] T. M. Brushart, *Nerve Repair*. Oxford University Press, 2011.

[14] A.-L. Cattin and A. C. Lloyd, 'The multicellular complexity of peripheral nerve regeneration', *Current Opinion in Neurobiology*, vol. 39, pp. 38–46, Aug. 2016, doi: 10.1016/j.conb.2016.04.005.

[15] E. A. Huebner and S. M. Strittmatter, 'Axon Regeneration in the Peripheral and Central Nervous Systems', *Results Probl Cell Differ*, vol. 48, pp. 339–351, 2009, doi: 10.1007/400_2009_19.

[16] T. Gordon, 'Peripheral Nerve Regeneration and Muscle Reinnervation', *International Journal of Molecular Sciences*, vol. 21, no. 22, Art. no. 22, Jan. 2020, doi: 10.3390/ijms21228652.

[17] A. D. Gaudet, P. G. Popovich, and M. S. Ramer, 'Wallerian degeneration: gaining perspective on inflammatory events after peripheral nerve injury', *Journal of Neuroinflammation*, vol. 8, no. 1, p. 110, Aug. 2011, doi: 10.1186/1742-2094-8-110.

[18] P. J. Arthur-Farraj *et al.*, 'c-Jun Reprograms Schwann Cells of Injured Nerves to Generate a Repair Cell Essential for Regeneration', *Neuron*, vol. 75, no. 4, pp. 633–647, Aug. 2012, doi: 10.1016/j.neuron.2012.06.021.

[19] S. Geuna *et al.*, 'Histology of the Peripheral Nerve and Changes Occurring During Nerve Regeneration', *International review of Neurobiology*, vol. 87, Accessed: June 24, 2025. [Online]. Available: https://www.academia.edu/12438835/Chapter_3_Histology_of_the_Peripheral_Nerve_and_Changes_Occurring_During_Nerve_Regeneration?auto=download

[20] G. Ronchi, F. Fregnan, L. Muratori, G. Gambarotta, and S. Raimondo, 'Morphological Methods to Evaluate Peripheral Nerve Fiber Regeneration: A Comprehensive Review', *International Journal of Molecular Sciences*, vol. 24, no. 3, Art. no. 3, Jan. 2023, doi: 10.3390/ijms24031818.

[21] A. Höke, 'Mechanisms of Disease: what factors limit the success of peripheral nerve regeneration in humans?', *Nat Rev Neurol*, vol. 2, no. 8, pp. 448–454, Aug. 2006, doi: 10.1038/ncpneuro0262.

[22] R. Schmidhammer, R. Rosenauer, and T. Hausner, 'Surgical Techniques in Nerve Repair', in *Peripheral Nerve Tissue Engineering and Regeneration*, J. B. Phillips, D. Hercher, and T. Hausner, Eds, in Reference Series in Biomedical Engineering. , Cham: Springer International Publishing, 2022, pp. 467–490. doi: 10.1007/978-3-030-21052-6_13.

[23] M. Szynkaruk, S. W. P. Kemp, M. D. Wood, T. Gordon, and G. H. Borschel, 'Experimental and Clinical Evidence for Use of Decellularized Nerve Allografts in Peripheral Nerve Gap Reconstruction', *Tissue Engineering Part B: Reviews*, vol. 19, no. 1, pp. 83–96, Feb. 2013, doi: 10.1089/ten.teb.2012.0275.

[24] E. Stocco *et al.*, 'Bridging Gaps in Peripheral Nerves: From Current Strategies to Future Perspectives in Conduit Design', *International Journal of Molecular Sciences*, vol. 24, no. 11, Art. no. 11, Jan. 2023, doi: 10.3390/ijms24119170.

[25] S. Geuna *et al.*, 'Schwann-Cell Proliferation in Muscle-Vein Combined Conduits for Bridging Rat Sciatic Nerve Defects', *J reconstr Microsurg*, vol. 19, no. 2, pp. 119–123, 2003, doi: 10.1055/s-2003-37818.

[26] T. Manoli *et al.*, 'Correlation analysis of histomorphometry and motor neurography in the median nerve rat model', *Eplasty*, vol. 14, p. e17, 2014.

[27] M. H. Levine, K. E. Yates, and L. B. Kaban, 'Nerve growth factor is expressed in rat femoral vein', *Journal of Oral and Maxillofacial Surgery*, vol. 60, no. 7, pp. 729–733, July 2002, doi: 10.1053/joms.2002.33237.

[28] A. Pagnotta, P. Tos, M. Fornaro, A. Gigante, S. Geuna, and B. Battiston, 'Neurotrophins and their receptors in early axonal regeneration along muscle-vein-combined grafts', *Microsurgery*, vol. 22, no. 7, pp. 300–303, 2002, doi: 10.1002/micr.10053.

[29] M. Stößel *et al.*, 'Comparative Evaluation of Chitosan Nerve Guides with Regular or Increased Bendability for Acute and Delayed Peripheral Nerve Repair: A Comprehensive Comparison with Autologous Nerve Grafts and Muscle-in-Vein Grafts', *The Anatomical Record*, vol. 301, no. 10, pp. 1697–1713, Oct. 2018, doi: 10.1002/ar.23847.

[30] K. S. Bhangra, F. Busuttil, J. B. Phillips, and A. A. Rahim, 'Using Stem Cells to Grow Artificial Tissue for Peripheral Nerve Repair', *Stem Cells International*, vol. 2016, no. 1, p. 7502178, 2016, doi: 10.1155/2016/7502178.

[31] M. S. Namini *et al.*, 'Cell-free therapy based on extracellular vesicles: a promising therapeutic strategy for peripheral nerve injury', *Stem Cell Res Ther*, vol. 14, no. 1, p. 254, Sept. 2023, doi: 10.1186/s13287-023-03467-5.

[32] Y. Izhiman and L. Esfandiari, 'Emerging role of extracellular vesicles and exogenous stimuli in molecular mechanisms of peripheral nerve regeneration', *Front Cell Neurosci*, vol. 18, p. 1368630, Mar. 2024, doi: 10.3389/fncel.2024.1368630.

[33] C.-Y. Liu *et al.*, 'Effect of exosomes from adipose-derived stem cells on the apoptosis of Schwann cells in peripheral nerve injury', *CNS Neuroscience & Therapeutics*, vol. 26, no. 2, pp. 189–196, 2020, doi: 10.1111/cns.13187.

[34] S. A. A. Kooijmans, C. G. Aleza, S. R. Roffler, W. W. Van Solinge, P. Vader, and R. M. Schiffelers, 'Display of GPI-anchored anti-EGFR nanobodies on extracellular vesicles promotes tumour cell targeting', *J of Extracellular Vesicle*, vol. 5, no. 1, Jan. 2016, doi: 10.3402/jev.v5.31053.

[35] G. Ronchi *et al.*, 'The Median Nerve Injury Model in Pre-clinical Research – A Critical Review on Benefits and Limitations', *Front. Cell. Neurosci.*, vol. 13, June 2019, doi: 10.3389/fncel.2019.00288.

[36] X. Navarro, 'Functional evaluation of peripheral nerve regeneration and target reinnervation in animal models: a critical overview', *Eur J of Neuroscience*, vol. 43, no. 3, pp. 271–286, Feb. 2016, doi: 10.1111/ejn.13033.

[37] H. M. Kaplan, P. Mishra, and J. Kohn, 'The overwhelming use of rat models in nerve regeneration research may compromise designs of nerve guidance conduits for humans', *J Mater Sci: Mater Med*, vol. 26, no. 8, p. 226, Aug. 2015, doi: 10.1007/s10856-015-5558-4.

[38] H. Wang, E. J. Sorenson, R. J. Spinner, and A. J. Windebank, 'Electrophysiologic findings and grip strength after nerve injuries in the rat forelimb', *Muscle Nerve*, vol. 38, no. 4, pp. 1254–1265, Oct. 2008, doi: 10.1002/mus.20971.

[39] F. Werdin *et al.*, 'An improved electrophysiological method to study peripheral nerve regeneration in rats', *Journal of Neuroscience Methods*, vol. 182, no. 1, pp. 71–77, Aug. 2009, doi: 10.1016/j.jneumeth.2009.05.017.

[40] K. Haastert-Talini, 'Appropriate Animal Models for Translational Nerve Research', in *Peripheral Nerve Tissue Engineering and Regeneration*, J. Phillips, D. Hercher, and T. Hausner, Eds, Cham: Springer International Publishing, 2020, pp. 1–17. doi: 10.1007/978-3-030-06217-0_9-1.

[41] R. Mihai, I. Florescu, V. Coroiu, A. Oancea, and M. Lungu, 'In vitro biocompatibility testing of some synthetic polymers used for the achievement of nervous conduits', *J Med Life*, vol. 4, no. 3, pp. 250–255, Aug. 2011.

[42] D. Angius, H. Wang, R. J. Spinner, Y. Gutierrez-Cotto, M. J. Yaszemski, and A. J. Windebank, 'A systematic review of animal models used to study nerve regeneration in tissue-engineered scaffolds', *Biomaterials*, vol. 33, no. 32, pp. 8034–8039, Nov. 2012, doi: 10.1016/j.biomaterials.2012.07.056.

[43] M. Barrot, 'Tests and models of nociception and pain in rodents', *Neuroscience*, vol. 211, pp. 39–50, June 2012, doi: 10.1016/j.neuroscience.2011.12.041.

[44] K. Hargreaves, R. Dubner, F. Brown, C. Flores, and J. Joris, 'A new and sensitive method for measuring thermal nociception in cutaneous hyperalgesia', *Pain*, vol. 32, no. 1, pp. 77–88, Jan. 1988, doi: 10.1016/0304-3959(88)90026-7.

[45] J. Heinzel *et al.*, 'Use of the CatWalk gait analysis system to assess functional recovery in rodent models of peripheral nerve injury – a systematic review', *Journal of Neuroscience Methods*, vol. 345, p. 108889, Nov. 2020, doi: 10.1016/j.jneumeth.2020.108889.

[46] J. C. Heinzel *et al.*, 'Evaluation of Functional Recovery in Rats After Median Nerve Resection and Autograft Repair Using Computerized Gait Analysis', *Front. Neurosci.*, vol. 14, Jan. 2021, doi: 10.3389/fnins.2020.593545.

[47] J. A. Bertelli and J. C. Mira, 'The grasping test: a simple behavioral method for objective quantitative assessment of peripheral nerve regeneration in the rat', *Journal of Neuroscience Methods*, vol. 58, no. 1–2, pp. 151–155, May 1995, doi: 10.1016/0165-0270(94)00169-H.

[48] M. Stößel, L. Rehra, and K. Haastert-Talini, 'Reflex-based grasping, skilled forelimb reaching, and electrodiagnostic evaluation for comprehensive analysis of functional recovery—The 7-mm rat median nerve gap repair model revisited', *Brain and Behavior*, vol. 7, no. 10, p. e00813, Sept. 2017, doi: 10.1002/brb3.813.

[49] C. L. A. M. Vleggeert-Lankamp, 'The role of evaluation methods in the assessment of peripheral nerve regeneration through synthetic conduits: a systematic review: Laboratory investigation', *JNS*, vol. 107, no. 6, pp. 1168–1189, Dec. 2007, doi: 10.3171/JNS-07/12/1168.

[50] D. Casal *et al.*, 'Reconstruction of a 10-mm-long median nerve gap in an ischemic environment using autologous conduits with different patterns of blood supply: A

comparative study in the rat', *PLoS ONE*, vol. 13, no. 4, p. e0195692, Apr. 2018, doi: 10.1371/journal.pone.0195692.

[51] N. Sinis, C. Schulte-Eversum, M. Doser, and H.-W. Müller, 'Nerve regeneration across a 2-cm gap in the rat median nerve using a resorbable nerve conduit filled with Schwann cells', *J. Neurosurg.*, vol. 103, 2005.

[52] S. Raimondo, M. Fornaro, F. Di Scipio, G. Ronchi, M. G. Giacobini-Robecchi, and S. Geuna, 'Chapter 5 Methods and Protocols in Peripheral Nerve Regeneration Experimental Research', in *International Review of Neurobiology*, vol. 87, Elsevier, 2009, pp. 81–103. doi: 10.1016/S0074-7742(09)87005-0.

[53] V. Carriel, I. Garzón, M. Alaminos, and M. Cornelissen, 'Histological assessment in peripheral nerve tissue engineering', *Neural Regen Res*, vol. 9, no. 18, pp. 1657–1660, Sept. 2014, doi: 10.4103/1673-5374.141798.

[54] F. D. Scipio, S. Raimondo, P. Tos, and S. Geuna, 'A simple protocol for paraffin-embedded myelin sheath staining with osmium tetroxide for light microscope observation', *Microscopy Res & Technique*, vol. 71, no. 7, pp. 497–502, July 2008, doi: 10.1002/jemt.20577.

[55] D. B. Parkinson *et al.*, 'c-Jun is a negative regulator of myelination', *The Journal of Cell Biology*, vol. 181, no. 4, pp. 625–637, May 2008, doi: 10.1083/jcb.200803013.

[56] S. C. Daeschler *et al.*, 'Rapid, automated nerve histomorphometry through open-source artificial intelligence', *Sci Rep*, vol. 12, no. 1, p. 5975, Apr. 2022, doi: 10.1038/s41598-022-10066-6.

[57] J. Lopez *et al.*, 'Growth Hormone Improves Nerve Regeneration, Muscle Re-innervation, and Functional Outcomes After Chronic Denervation Injury', *Scientific Reports*, vol. 9, p. 3117, Feb. 2019, doi: 10.1038/s41598-019-39738-6.

[58] R. Fitzhugh, 'Theoretical Effect of Temperature on Threshold in the Hodgkin-Huxley Nerve Model', *J Gen Physiol*, vol. 49, no. 5, pp. 989–1005, May 1966, doi: 10.1085/jgp.49.5.989.

[59] A. Zaimi, M. Wabartha, V. Herman, P.-L. Antonsanti, C. S. Perone, and J. Cohen-Adad, 'AxonDeepSeg: automatic axon and myelin segmentation from microscopy data using convolutional neural networks', *Sci Rep*, vol. 8, no. 1, p. 3816, Feb. 2018, doi: 10.1038/s41598-018-22181-4.

[60] G. Landini, G. Martinelli, and F. Piccinini, 'Colour deconvolution: stain unmixing in histological imaging', *Bioinformatics*, vol. 37, no. 10, pp. 1485–1487, June 2021, doi: 10.1093/bioinformatics/btaa847.

[61] A. D. C. Rodrigues, J. C. Andreo, G. M. R. Júnior, N. B. Dos Santos, L. H. R. Moraes, and J. R. P. Lauris, 'Fat cell invasion in long-term denervated skeletal muscle', *Microsurgery*, vol. 27, no. 8, pp. 664–667, Jan. 2007, doi: 10.1002/micr.20428.

[62] J. Isaacs, 'Major Peripheral Nerve Injuries', *Hand Clinics*, vol. 29, no. 3, pp. 371–382, Aug. 2013, doi: 10.1016/j.hcl.2013.04.006.

[63] Y. Li, J. Lao, X. Zhao, D. Tian, Y. Zhu, and X. Wei, 'The optimal distance between two electrode tips during recording of compound nerve action potentials in the rat median nerve', *Neural Regen Res*, vol. 9, no. 2, pp. 171–178, Jan. 2014, doi: 10.4103/1673-5374.125346.

[64] S. Geuna, P. Tos, B. Battiston, and M. G. Giacobini-Robecchi, 'Bridging peripheral nerve defects with muscle–vein combined guides', *Neurological Research*, vol. 26, no. 2, pp. 139–144, Mar. 2004, doi: 10.1179/016164104225013752.

[65] S. Geuna, P. Tos, B. Battiston, R. Guglielmone, and M. G. Giacobini-Robecchi, 'Morphological analysis of peripheral nerve regenerated by means of vein grafts filled with fresh skeletal muscle', *Anatomy and Embryology*, vol. 201, no. 6, pp. 475–482, May 2000, doi: 10.1007/s004290050334.

[66] B. Battiston, P. Tos, S. Geuna, M. G. Giacobini-Robecchi, and R. Guglielmone, 'Nerve repair by means of vein filled with muscle grafts. II. Morphological analysis of regeneration', *Microsurgery*, vol. 20, no. 1, pp. 37–41, 2000, doi: 10.1002/(SICI)1098-2752(2000)20:1<37::AID-MICR7>3.0.CO;2-5.

[67] S. V. Fazal *et al.*, 'Graded Elevation of c-Jun in Schwann Cells *In Vivo* : Gene Dosage Determines Effects on Development, Remyelination, Tumorigenesis, and Hypomyelination', *J. Neurosci.*, vol. 37, no. 50, pp. 12297–12313, Dec. 2017, doi: 10.1523/JNEUROSCI.0986-17.2017.

[68] K. R. Jessen and R. Mirsky, 'The Role of c-Jun and Autocrine Signaling Loops in the Control of Repair Schwann Cells and Regeneration', *Front Cell Neurosci*, vol. 15, p. 820216, Feb. 2022, doi: 10.3389/fncel.2021.820216.

[69] D. Triolo *et al.*, 'Loss of glial fibrillary acidic protein (GFAP) impairs Schwann cell proliferation and delays nerve regeneration after damage', *Journal of Cell Science*, vol. 119, no. 19, pp. 3981–3993, Oct. 2006, doi: 10.1242/jcs.03168.

[70] M. Fornaro, P. Tos, S. Geuna, M. G. Giacobini-Robecchi, and B. Battiston, 'Confocal imaging of Schwann-cell migration along muscle-vein combined grafts used to bridge nerve defects in the rat', *Microsurgery*, vol. 21, no. 4, pp. 153–155, 2001, doi: 10.1002/micr.1029.

[71] C. Cheng and D. W. Zochodne, '*In vivo* proliferation, migration and phenotypic changes of Schwann cells in the presence of myelinated fibers', *Neuroscience*, vol. 115, no. 1, pp. 321–329, Nov. 2002, doi: 10.1016/S0306-4522(02)00291-9.

[72] T. Tabarin *et al.*, 'Deep learning segmentation (AxonDeepSeg) to generate axonal-property map from ex vivo human optic chiasm using light microscopy', *Proceedings of the International Society for Magnetic Resonance in Medicine*, vol. 28, no. 2019, p. 4722, 2019.

[73] E. Ülkür, F. Yüksel, C. Açikel, İ. Okar, and B. Çeliköz, 'Comparison of functional results of nerve graft, vein graft, and vein filled with muscle graft in end-to-side neurorrhaphy', *Microsurgery*, vol. 23, no. 1, pp. 40–48, Jan. 2003, doi: 10.1002/micr.10076.

[74] S. Jonsson *et al.*, 'Effect of Delayed Peripheral Nerve Repair on Nerve Regeneration, Schwann Cell Function and Target Muscle Recovery', *PLoS ONE*, vol. 8, no. 2, p. e56484, Feb. 2013, doi: 10.1371/journal.pone.0056484.

[75] M. Ikeda and Y. Oka, 'The relationship between nerve conduction velocity and fiber morphology during peripheral nerve regeneration', *Brain and Behavior*, vol. 2, no. 4, pp. 382–390, 2012, doi: 10.1002/brb3.61.

[76] A. P. Santos, C. A. Suaid, V. P. S. Fazan, and A. A. Barreira, 'Microscopic anatomy of brachial plexus branches in Wistar rats', *The Anatomical Record*, vol. 290, no. 5, pp. 477–485, 2007, doi: 10.1002/ar.20519.

[77] C. A. Suaid, A. P. Santos, F. D. O. Yamane, V. P. S. Fazan, and A. A. Barreira, 'Aspects of the Macro and Microscopic Anatomy of the Sciatic Nerve in Wistar Rats', *Int. J. Morphol.*, vol. 34, no. 3, pp. 877–884, Sept. 2016, doi: 10.4067/S0717-95022016000300010.

[78] P. E. Barkhaus, S. D. Nandedkar, M. de Carvalho, M. Swash, and E. V. Stålberg, 'Revisiting the compound muscle action potential (CMAP)', *Clin Neurophysiol Pract*, vol. 9, pp. 176–200, May 2024, doi: 10.1016/j.cnp.2024.04.002.

[79] B. M. Carlson, 'The Biology of Long-Term Denervated Skeletal Muscle', *Eur J Transl Myol*, vol. 24, no. 1, p. 3293, Mar. 2014, doi: 10.4081/ejtm.2014.3293.

[80] A. Lysak, S. Farnebo, S. Geuna, and L. B. Dahlin, 'Muscle preservation in proximal nerve injuries: a current update', *J Hand Surg Eur Vol*, vol. 49, no. 6, pp. 773–782, June 2024, doi: 10.1177/17531934231216646.

A1 Appendix

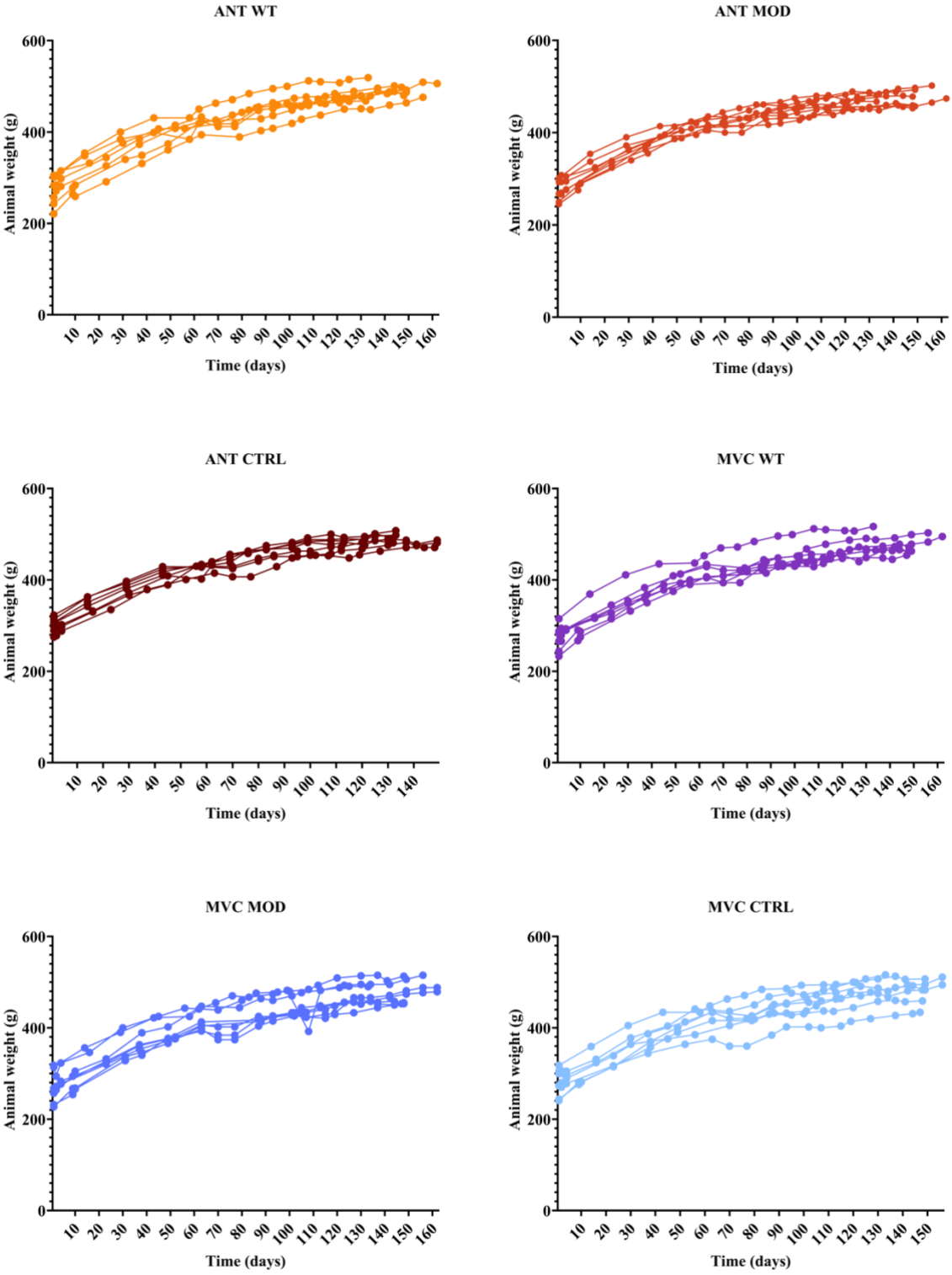

Fig. A1.1. Increase in body weight over time across treatment groups. Body weight trajectories of individual animals are shown for each treatment group (A-F).

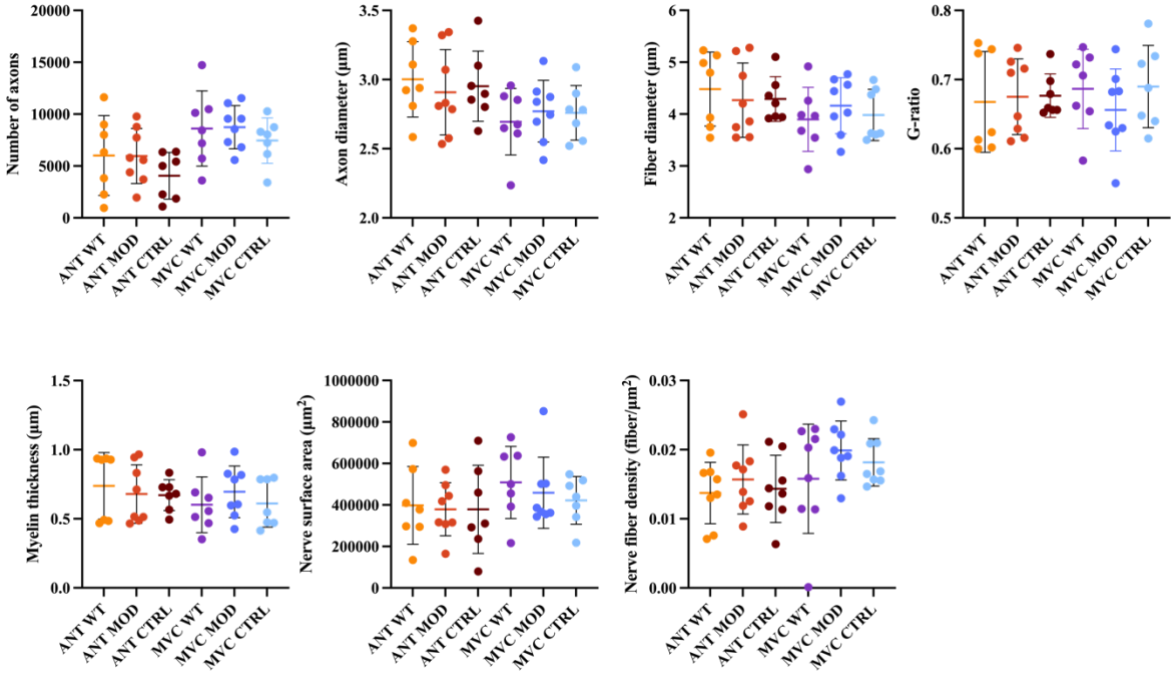

Fig. A1.2. Morphometrics of 6 treatment groups at the anatomical location proximal to injury (cut 1). (a) Number of axons, (b) axon diameter, (c) fiber diameter, (d) g-ratio, (e) myelin thickness, (f) nerve surface area, and (g) nerve fiber density. Statistical significance between ANT and MVC was assessed with the Kruskal-Wallis test followed by Dunn's multiple comparisons test (*p<0.05, **p<0.01, ***p<0.001 between ANT and MVC).

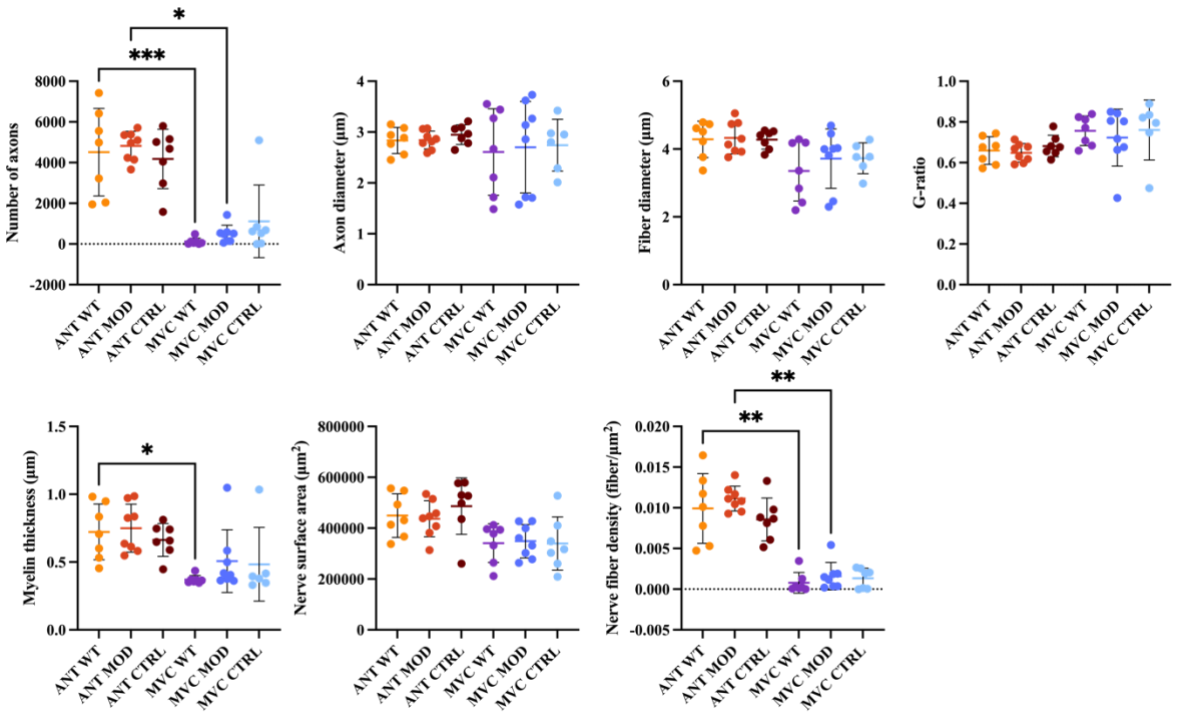

Fig. A1.3. Morphometrics of 6 treatment groups at the anatomical location proximal to middle of graft (cut 2). (a) Number of axons, (b) axon diameter, (c) fiber diameter, (d) g-ratio, (e) myelin thickness, (f) nerve surface area, and (g) nerve fiber density. Statistical significance between ANT and MVC was assessed with the Kruskal-Wallis test followed by Dunn's multiple comparisons test (*p<0.05, **p<0.01, ***p<0.001 between ANT and MVC).

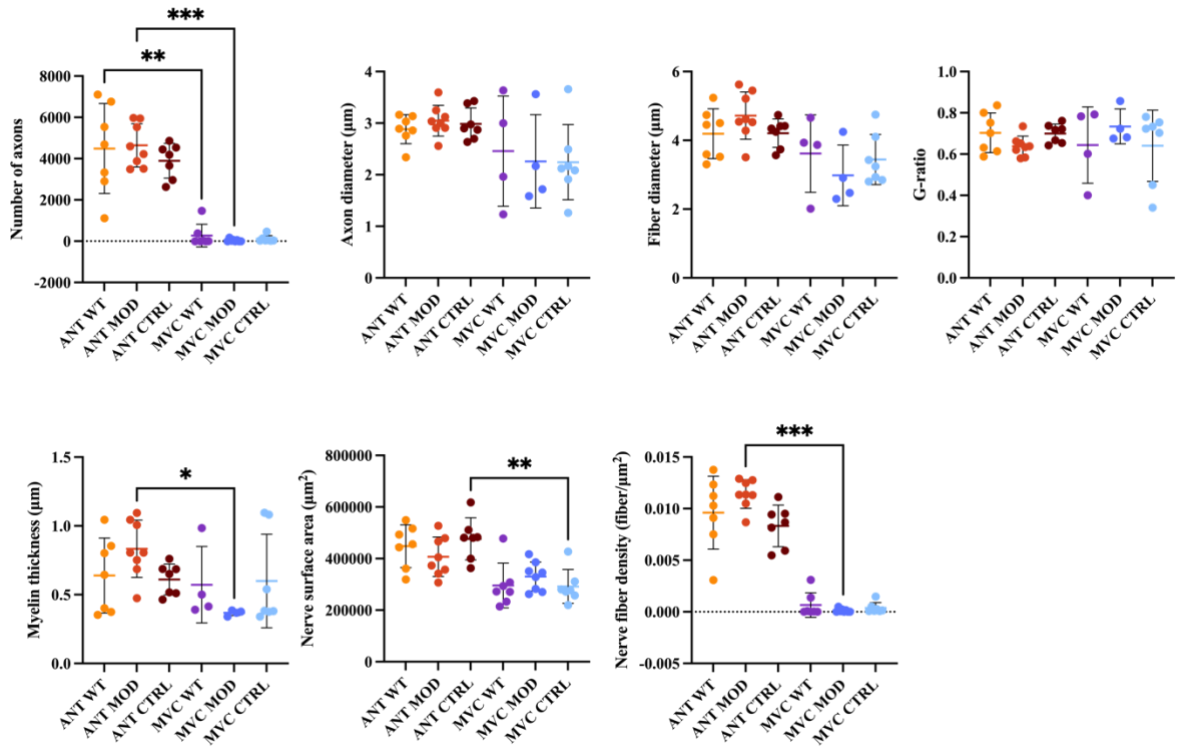

Fig. A1.4. Morphometrics of 6 treatment groups at the anatomical location distal to middle of the graft (cut 3). (a) Number of axons, (b) axon diameter, (c) fiber diameter, (d) g-ratio, (e) myelin thickness, (f) nerve surface area, and (g) nerve fiber density. Statistical significance between ANT and MVC was assessed with the Kruskal-Wallis test and Brown-Forsythe and Welch test followed by Dunn's and Dunnett's T3 multiple comparisons test (*p<0.05, **p<0.01, ***p<0.001 between ANT and MVC).

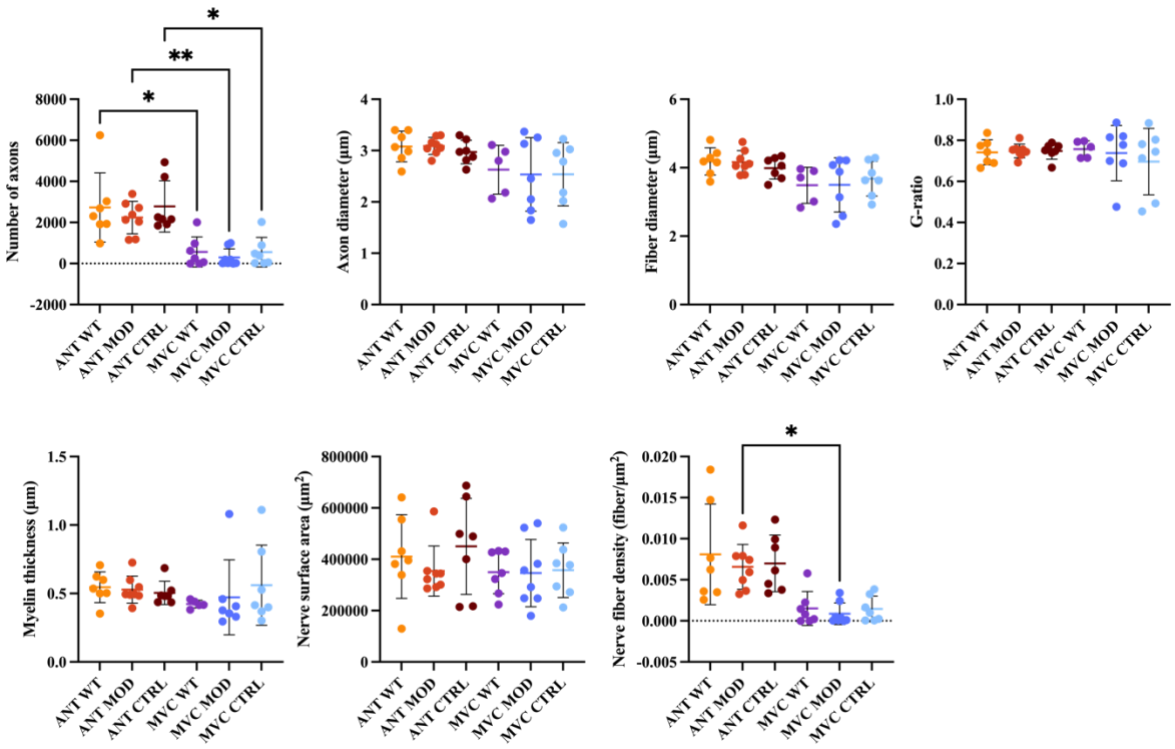

Fig. A1.5. Morphometrics of 6 treatment groups at the anatomical location distal to injury (cut 4). (a) Number of axons, (b) axon diameter, (c) fiber diameter, (d) g-ratio, (e) myelin thickness, (f) nerve surface area, and (g) nerve fiber density. Statistical significance between ANT and MVC was assessed with the Kruskal-Wallis test followed by Dunn's multiple comparisons test (*p<0.05, **p<0.01, ***p<0.001 between ANT and MVC).

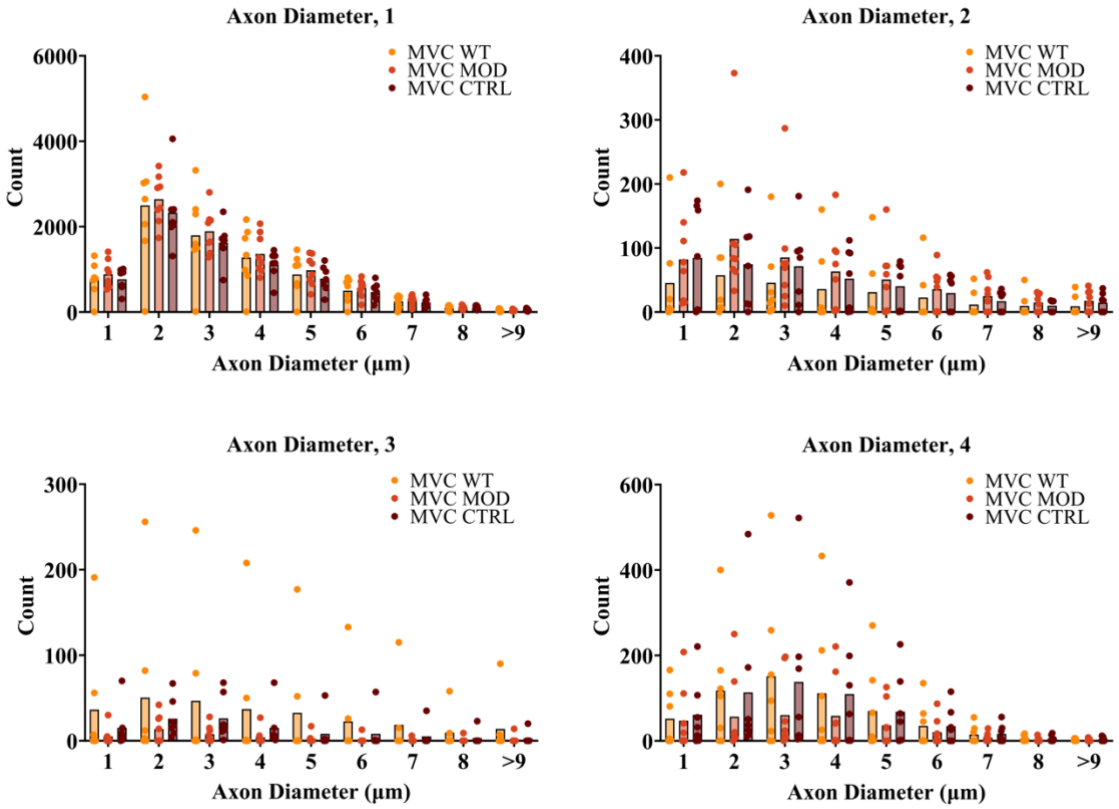

Fig. A1.6. Histogram of axon diameter at 4 anatomical locations for MVC.

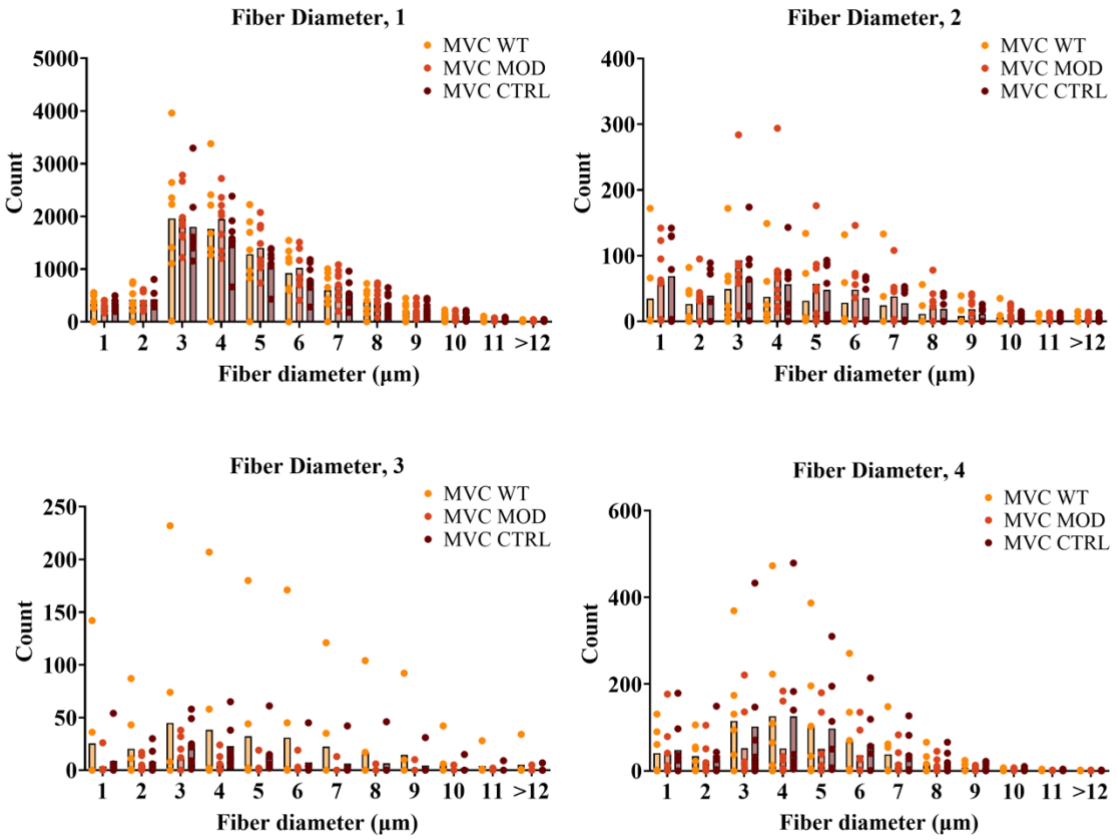

Fig. A1.7. Histogram of fiber diameter at 4 anatomical locations for MVC.

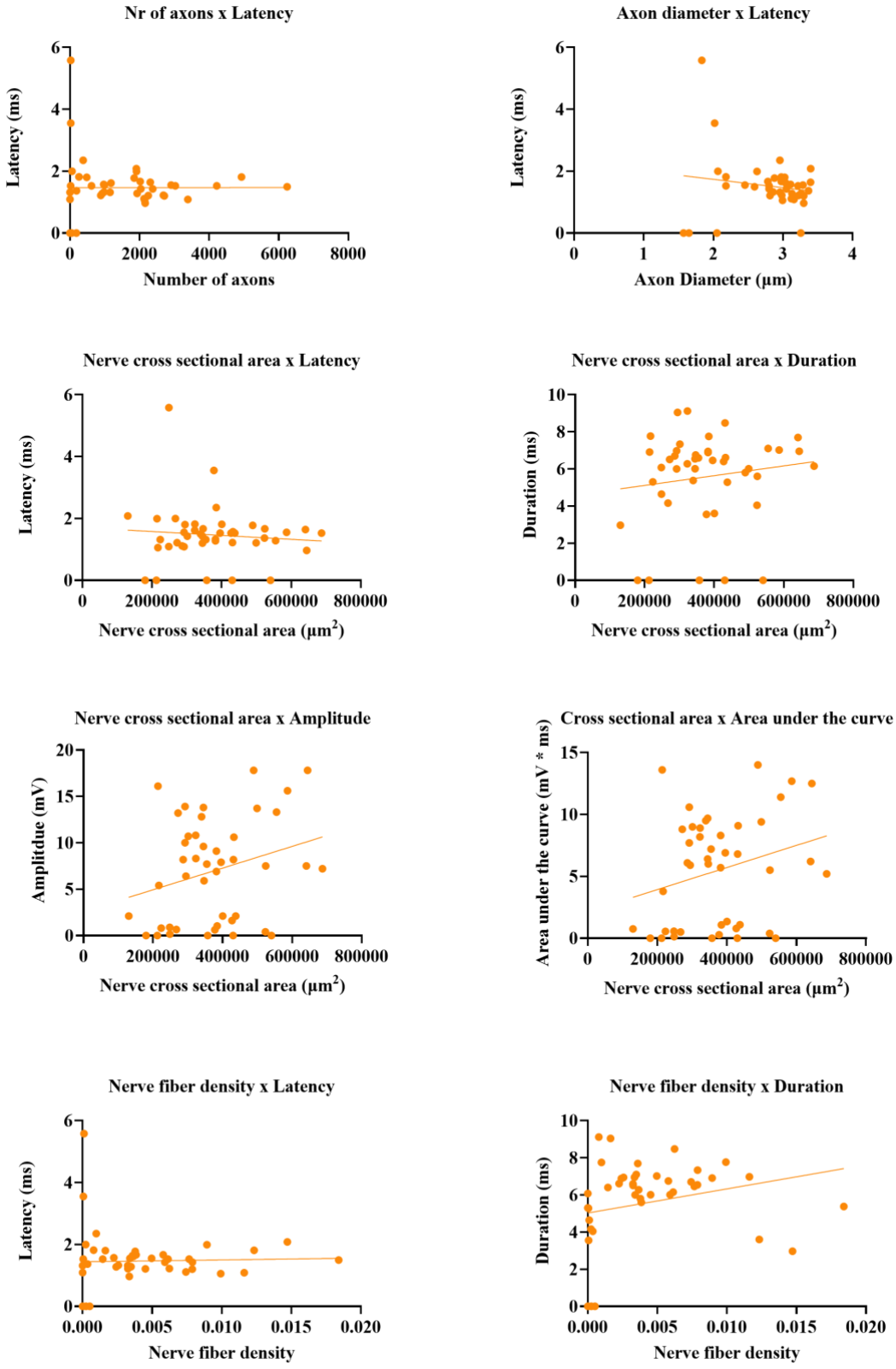

Fig. A1.8. Non-statistically significant correlations between neurographic and histomorphometric parameters. Including number of axons, axon diameter, nerve cross sectional area, and nerve fiber density.

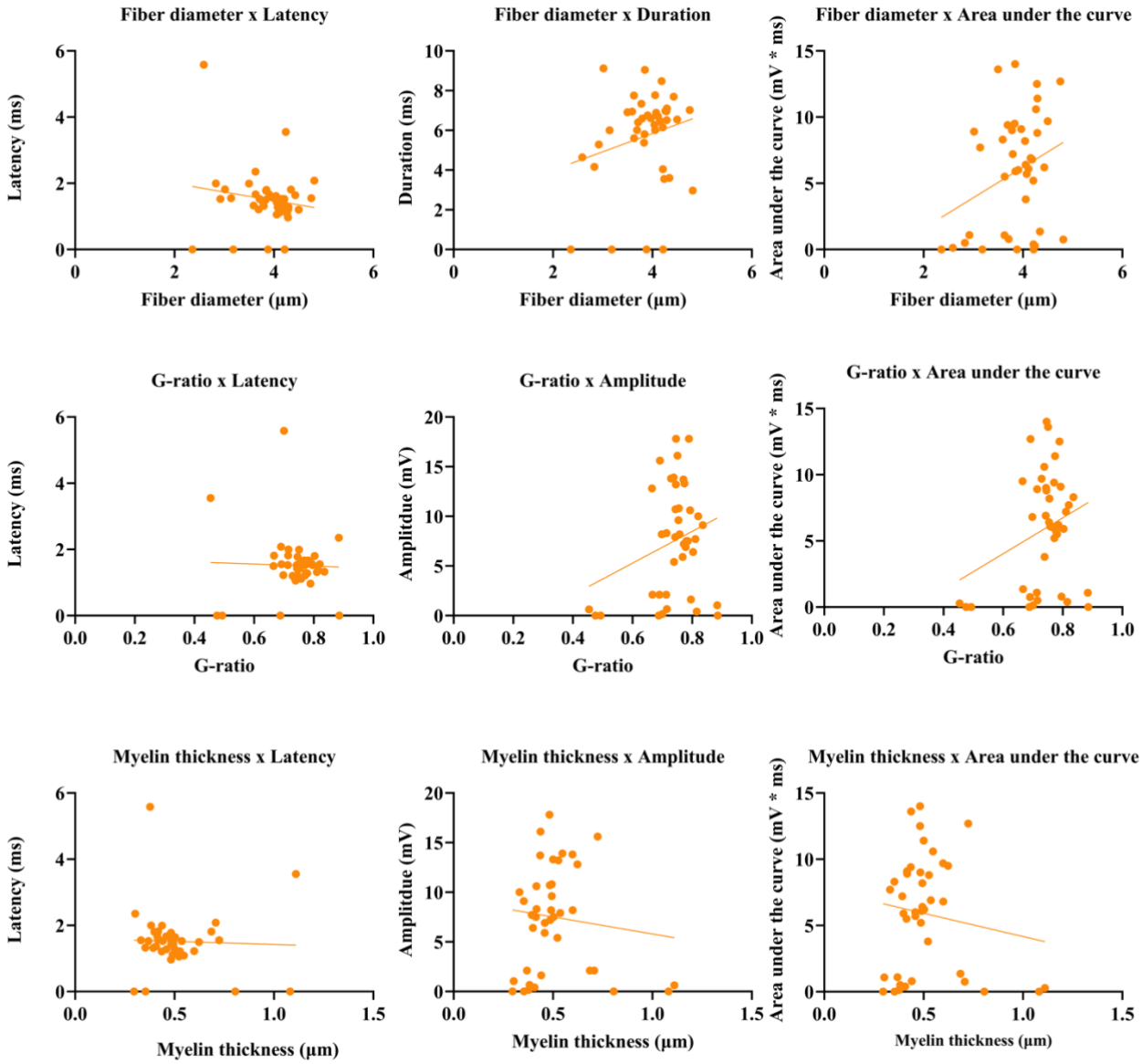

A1.9. Non-statistically significant correlations between neurographic and histomorphometric parameters. Including fiber diameter, g-ratio, and myelin thickness.

Table A1.1: Overview of animals used for representative images in each figure.

	ANT WT	ANT MOD	ANT CTRL	MVC WT	MVC MOD	MVC CTRL
H&E (Fig. 7)	AE7830 ~ E2R38	AE7833 ~ E2R41	AE7802 ~ E2R10	AE7816 ~ E2R24	AE7803 ~ E2R11	AE7813 ~ E2R21
c-JUN (Fig. 8)	AE7830 ~ E2R38	AE7798 ~ E2R6	AE7802 ~ E2R10	AE7816 ~ E2R24	AE7803 ~ E2R11	AE7813 ~ E2R21
GFAP (Fig. 9)	AE7830 ~ E2R38	AE7839 ~ E2R47	AE7802 ~ E2R10	AE7828 ~ E2R36	AE7803 ~ E2R11	AE7826 ~ E2R34
MBP (Fig. 10)	AE7830 ~ E2R38	AE7833 ~ E2R41	AE7802 ~ E2R10	AE7816 ~ E2R24	AE7806 ~ E2R14	AE7813 ~ E2R21
MSB (Fig. 15)	AE7830 ~ E2R38	AE7833 ~ E2R41	AE7802 ~ E2R10	AE7816 ~ E2R24	AE7806 ~ E2R14	AE7813 ~ E2R21